# The last 30,000 to 700,000 years ago: Unravelling the timing of human settlement for the Palaeolithic site of Kozarnika

Maryam Heydari, Guillaume Guérin, Nikolay Sirakov, Philippe Fernandez, Catherine Ferrier, Aleta Guadelli, Jean-Claude Leblanc, Stanimira Taneva, Svoboda Sirakova, Jean-Luc Guadelli

To be submitted to the journal of Quaternary Science Reviews

# The last 30,000 to 700,000 years ago: unravelling the timing of human settlement for the Palaeolithic site of Kozarnika

Maryam Heydari[1,2]*, Guillaume Guérin[2,3], Nikolay Sirakov[4], Philippe Fernandez[5], Catherine Ferrier[6], Aleta Guadelli[7], Jean-Claude Leblanc[8], Stanimira Taneva[4], Svoboda Sirakova[4] and Jean-Luc Guadelli[6]

[1]Institute of Earth and Environmental Sciences, University of Freiburg, Albertstr. 23b, 79104 Freiburg, Germany
[2]IRAMAT-CRP2A, UMR 5060, CNRS-Universite Bordeaux Montaigne, Maison de l'archéologie, Esplanade des Antilles, 33607 Pessac cedex, France
[3]Université de Rennes, CNRS, Géosciences Rennes, UMR 6118, 35000 Rennes, France
[4]National Institute of Archaeology with Museum-Bulgarian Academy of Sciences, 2, Saborna Street, 1000 Sofia, Bulgaria
[5]CNRS, Aix Marseille Univ, Minist Culture, LAMPEA UMR 7269, Maison Mediterraneenne des Sciences de l'Homme, 5 Rue du Chateau de l'Horloge BP 647, F13094, Aix-en-Provence, France
[6]PACEA-UMR5199 CNRS, Université de Bordeaux, Allée Geoffroy Saint Hilaire, Bâtiment B18, CS50023, 33615 Pessac Cedex, France
[7]National Institute of Immovable Cultural Heritage, Latchezar Stanchev Street 7, 1125 Sofia, Bulgaria
[8]TRACES-UMR5608 CNRS, Université de Toulouse le Mirail, Maison de La Recherche, 5, Allées Antonio Machado, 31048 Toulouse Cedex 1, France

*Corresponding author: mariheyd@gmail.com

**Abstract**

Kozarnika cave is a renowned prehistoric site in the Balkans, which contributes significantly to our understanding of the human past due to its rich assemblages associated with the Lower to Upper palaeolithic periods. To unravel the timing of human occupations in Kozarnika, various dating methods have been employed in the past. Radiocarbon dating was used to unfold the timeframe for the Kozarnikian lithic tradition uncovered in the Upper Palaeolithic sequence of the cave, and paleomagnetic dating assigned the Brunhes–Matuyama reversal to the layer beneath the Lower Palaeolithic assemblages.

In this study, we employed luminescence-dating methods including a body of different signals to date sediment layers from the top to the bottom of the sequence covering the period of ca 30 to 700 ka. Our investigations revealed that the Kozarnikian tradition in layers 5a-c falls between 30–35 ka. Following that, we suggest that the Middle Palaeolithic period initiated between 250–309 ka and lasted until 40–53 ka. More importantly, we have updated the age of the Neanderthal radius discovered in the Mousterian assemblages to 201±17 ka.

Our dating of the Lower Palaeolithic assemblages in the cave rendered the period of ca 300-700 ka. Taking into account the timeframe suggested by the paleomagnetic sequence <780 ka it is likely that we have reached the threshold of the luminescence dating method and the age range may represent the minimum age for this period.

## 1. Introduction

The Balkans are renowned for witnessing different hominin and human species of inhabitants due to the location between the Near East and the Western Europe during the long period of the Palaeolithic. Human remains associated with the Neanderthals or anatomically modern humans (AMH) have been discovered in the Middle and Upper palaeolithic assemblages in various sites (e.g., Galanidou, 2004; Glen and Kaczanowski, 1982; Hoffecker, 2009; Hublin et al., 2020; Strait et al., 2016; Tillier et al., 2017). Additionally, the high possibility of interaction between two human species (Fu et al., 2015; Hajdinjak et al., 2021) renders this region unique for further investigations.

Establishing a reliable temporal framework disclosing the timing of hominin species' settlements, the demise of one (e.g., Neanderthal), and domination of another (e.g., AMH) is a fundamental study, and it can be revealed through applying numerical dating methods. Among the whole body of techniques, radiocarbon dating plays a major role to track dynamics of the human peopling during the Late Middle to Upper Palaeolithic periods generally for Europe (e.g., Higham et al., 2014) and in particular for the Balkans (e.g., Alex et al., 2019; Devièse et al., 2017; Fewlass et al., 2020; Higham et al., 2006.; Trinkaus et al., 2003).

Whilst numerous temporal frameworks have been constructed to date the humans' fossils or the artefacts attributed to the Middle/Upper Palaeolithic, the number of available datasets is relatively scarce for the Lower to Middle Palaeolithic. This could be explained due to the shortage of the well-preserved Lower Palaeolithic sequences in eastern Europe (Doronichev, 2008). Having said that, the Palaeolithic site of Kozarnika has been a special place all along not only because of its rich archaeological remains related to the Lower Palaeolithic but also for offering the first Bulgarian Neanderthal's remain, a radius associated with a rich Mousterian assemblage (Tillier et al., 2017). Furthermore, the Upper palaeolithic industry found in the cave stands out from the other lithic productions and is known as *Kozarnikian* (Guadelli et al., 2005; Tsanova, 2006; Sirakov et al., 2007).

During the last decades, different dating methods have been employed to establish reliable chronologies for the sequences in the cave. The Upper Palaeolithic sequence was dated using the radiocarbon method (Guadelli et al., 2005, in press). Moreover, preliminary luminescence

ages attributed to the neanderthal radius were previously published (Tillier et al., 2017). In another study, a palaeomagnetism sequence was established for stratified layers in Kozarnika (Muttoni et al., 2017). Finally, a timeframe for the Lower and Middle Palaeolithic assemblages was demonstrated on mammal biochronology (Guadelli et al., 2005, in press; Fernandez and Cregut-Bonnoure, 2007; Popov and Marinska, 2007; Sirakov et al., 2010).

In this study, we applied multiple luminescence-dating methods not only to elucidate the timeframe of humans resided during the Middle and Upper Palaeolithic but to shed light on the timing of the inhabitants at the Lower Palaeolithic and provide a full chronology covering the complete sequence through sediment samples. This will allow us to improve our understanding about the timing of humans' settlements, particularly for Kozarnika and more widely for the Balkans.

### 1.1 Site location

Kozarnika cave is located in the northwest of Bulgaria, 30 km away from the Serbian border (Fig. 1). The site is situated in the northern slopes of the Balkan Mountains, merging to the Danubian Plain, which is extended to the Danube River to the north. The cave is positioned at an altitude of 481 m on the mountainside of Bashovishka Bara valley. The streams in the valley drain into the Skomlia River irrigating the region, which feeds the Danube River ca 30 km away.

The first report about Kozarnika dates back to 1933 (Popov (Попов), 1933) and years after in 1996, the site was excavated systematically by Bulgarian-French researchers (Guadelli et al., 2005). Following years of collaborative work, 21 geological layers were discovered in a sequence of about 9 m containing assemblages attributed to the Lower, Middle, Upper Palaeolithic as well as Holocene.

Fig. 1.

### 1.2 Stratified geological layers including archaeological discoveries

The Bashovishka Bara valley has cut 185 m deep into the northern foothills of the Balkan through three main geological formations. The top formation belongs to the Early Jurassic which at the middle is replaced by the Middle Jurassic and finally at the bottom is superimposed on the Late Jurassic. The Kozarnika cave consists mainly of limestone, which is formed in the Upper Jurassic geological formation (Guadelli et al., 2005; Sirakov et al., 2010). The cave is part of a larger karst landscape with other caves discovered in the north-western region of Bulgaria.

110 The Pleistocene layers in the cave are generally well-preserved. However, we observed
111 truncations in the cave for some layers containing Middle and Upper Palaeolithic assemblages
112 (Guadelli et al., 2005; Sirakov et al., 2010). These truncations are likely stemming from the
113 cave's subsequent use in modern times, when it was used as a mushroom farm and goat farm,
114 and finally as a bunker in the 1960s.
115 The geological layers in the cave were categorised into four main groups covering the top to
116 the bottom of the excavation profile (Fig. 2). Their general characteristics are explained below.
117
118 Fig. 2.
119
120
121 **1.3 Geological layers containing the archaeological finds**
122 **Layers 3a-4.** These layers with a thickness of 1 m to 1.4 m form the top of the sequence. Most
123 of the sediment is of aeolian origin. Nevertheless, a considerable amount of calcareous clasts
124 gravels in colours from light brown to whitish silty medium can be found in this part in addition
125 to debris from the ceiling and the walls of the cave. The archaeological assemblages belong to
126 the middle and late Kozarnikian tradition (the indigenous eponymous bladelets industry
127 mentioned above) associated with the Upper Palaeolithic (Guadelli et al., 2005).
128 **Layer 5a-10a.** These layers show thicknesses of 1.2-1.5 m and were deposited through a
129 combination of aeolian transport (recognised by beige silty-fine grains), and sediment
130 fragments from the ceiling and walls (identified with coarse grains and calcareous gravel and
131 pebble). Both groups of sediments are distributed irregularly over the section. Layer 5b
132 contains some volcanic ashes superimposed on layers 6 and 7, which both were composed of
133 silty sediment varying from light grey (6) to light brown (7). Due to the similarity between the
134 origin of these two layers, they both were considered as one layer named 6/7. The calcareous
135 gravels and charcoal also were sparsely observed in this layer (Ferrier et al., 2009). Generally
136 speaking, the formation of layers 5a, 6/7, and 10a is dominated by aeolian processes. Layers
137 10a-9a contain archaeological elements related to the Middle Palaeolithic period. The
138 archaeological finds in layer 6/7 are consistent with the Middle and Initial Upper Palaeolithic
139 assemblages. The upper layer (5a) contains the blade industry known as the Kozarnikian
140 tradition.
141 **Layer 10b-10c.** These layers originated from roughly weathered calcareous gravel and
142 pebbles, with a combination of loamy sand with dark brown colour that could be attributed to
143 human activity in the past. The sediment thicknesses of these layers vary from 15 cm to 50 cm

and contain archaeological artefacts associated with the very early Middle Palaeolithic with the Mousterian characteristics.

**Layer 11a-13.** These layers were located at the bottom of the sequence having a thickness of ca 2.5 m. The sediments in this section consist of orange loamy fine and coarse fractions with flint, limestone, and debris from the ceiling and the walls of the cave. In particular calcareous pebbles and blocks with various concentrations were observed in layer11a as a common feature of this layer in a different part of the cave. The same pattern with a combination of a dark fraction of silty material with quartz origin applies for layers 11b, 11c, 12, and 13. It is likely that this sequence of layers is a result of mudslides according to Ferrier et al. (2009). All of these layers comprise findings from an industry affiliated with the Lower Palaeolithic period.

## 2. Material and Methods

Luminescence dating estimates energy (radiation dose) deposited in natural minerals after the last sunlight exposure. This quantity is known as the equivalent dose (estimated in the laboratory), which is built up by energy emitted by natural radioelements in the sediment over the burial time (dose rate). Dividing the equivalent dose by the corresponding dose rate, results in the burial time (age). We used various techniques to determine the equivalent doses of the samples. First, we began with the blue optically stimulated luminescence (OSL) for quartz (Huntley et al., 1985), followed by post infrared stimulated luminescence at the elevated temperature ( Post-IR IRSL, Thomsen et al., 2008) to completely cover the Middle to the Upper palaeolithic sequences. In addition, the infrared stimulated luminescence (IRSL, Hütt et al., 1988) signals for some samples were measured at 50 ˚C to crosscheck with the two other age series.

It is well-known that signal saturation is a key parameter hampering the application of luminescence dating for the Lower to Middle Palaeolithic. Given that, we attempted to tackle this problem by combining various luminescence signals with different saturation degrees to extend the age limit. We switched to violet stimulated luminescence (VSL) (Ankjærgaard et al., 2016, 2013; Jain, 2009) on quartz accompanied by infrared radiofluorescence (IR-RF) (Trautmann et al., 1999b, 1999a, 1998, for review see Murari et al., 2021) on K-feldspar to estimate ages for the older samples.

The dose rates were estimated by means of both *in situ* and laboratory measurements for all samples (further details below).

### 2.1 Sample preparation

We present ages for 18 sediment samples extracted from the profile, using opaque tubes (see Table 1). Our sample preparation followed routine procedures applied in luminescence dating (Preusser et al., 2008). After conducting the grain size analysis (see Fig. S1 in the supplementary material) coarse grains with 180 μm to 250 μm diameters were extracted using wet sieving. To eliminate carbonates, the obtained fraction of sediments was rinsed in HCl (30%) over a couple of hours until no further reaction was observed. Following that, they were soaked in $H_2O_2$ (30%) to remove organic compounds. Later, density separation was carried out through lithium hetero-polytungstates (LST) heavy-liquid. First, quartz grains were separated from the bulk sample using a density of 2.62 g $cm^{-3}$. Then, K-feldspar grains were extracted from the remaining material by applying the LST with a density of 2.58 g $cm^{-3}$. We removed the outer layers of quartz and K-feldspar grains affected by alpha particles by etching them with HF; (40% for 40 min on quartz and 10% for 10 min on K-feldspar). Etching was followed by resting the grains in HCl (15%) overnight to eliminate unwanted fluorides. Finally, all grains were sieved for the second time with the smaller mesh size (<180 μm) to remove any remaining fragmented grains.

Table 1

**2.3 Instrumentation**

Various instruments were employed for measuring luminescence signals using different minerals and techniques. Blue OSL was measured on Freiberg Instrument lexsyg SMART TL/OSL systems (Richter et al., 2015) equipped with five blue LEDs (458 Δ 3 nm, max. 100 mW $cm^{-2}$) and five infrared LEDs (850 Δ 3 nm, max. 300 mW $cm^{-2}$) as well as on a Freiberg Instrument lexsyg research reader (hereafter L1,(Richter et al., 2013) equipped with five blue LEDs (458 Δ 10 nm, max. 100 mW $cm^{-2}$) and five infrared LEDs (850 Δ 3 nm, maximum 300 mW $cm^{-2}$). The stimulation powers for lexsyg research and lexsyg SMART systems were set to 100 $mWcm^{-2}$ and 40 $mWcm^{-2}$, respectively. Signals were detected using a UV filter combination (Hoya U340, 2.5 mm and Delta BP 365/50 EX) in both systems.

Post-IR IRSL ($pIR_{50}IRSL_{290}$) signal was measured using a blue-violet filter combination Schott BG 39 (3 mm) and Chroma D410/30x in Freiberg Instruments lexsyg research reader with a stimulation power of 100 $mWcm^{-2}$.

IRSL signals were measured using Risø TL/OSL DA-15 and DA-20 readers equipped with five blue LEDs (470 Δ 20 nm, max. 105 mW $cm^{-2}$) and five infrared LEDs (870 Δ 40 nm, max. 145 mW $cm^{-2}$). Signals were detected through a combination of Schott BG39 and Corning 7-59 (Bøtter-Jensen et al., 2003).

VSL signals were measured using Freiberg Instruments lexsyg research reader containing violet-emitting LEDs (405 Δ 3nm, max. 100 mW $cm^{-2}$). The stimulation power was set to 100 $mWcm^{-2}$ and the signal was detected using a combination of a Hoya U340 (2.5 mm) and an AHF-BL HC 340/26 interference filter.

All systems were operated with a $^{90}Sr/^{90}Y$- source which was calibrated using Risø calibration quartz (Hansen et al., 2015). The dose rates available for each sample in lexsyg research and SMART as well as Risø TL/OSL systems were ca 8 Gy $min^{-1}$, 11 $Gymin^{-1}$, and 7 Gy $min^{-1}$ at the measurement dates, respectively.

IR-RF was measured through another Freiberg Instrument lexsyg research system, which was equipped with a Hamamatsu H7421-50 PMT in conjunction with a Chroma D850/40 interference filter. A calibrated $^{90}Sr/^{90}Y$- source delivered a dose rate of ca 3 Gy $min^{-1}$. For the bleaching of the natural IR-RF, we used the internal solar simulator of the machine. All samples were prepared using stainless steel cups with a diameter of 8 mm.

Approximately, a hundred grains were mounted in diameter of 3 mm using silicon oil for measuring blue OSL, $pIR_{50}IRSL_{290}$, and IRSL. The number of grains was increased for VSL and IR-RF; in these cases, the cups were fully covered by grains, representing several thousand grains.

**2.4 Dose rate**

The dose rate available to quartz and feldspar consists of external and internal parts due to the activity of the radioelements outside and inside of the grains. For the external part, we have only estimated beta and gamma dose rates because the etching removed the outer layer of the grains affected by alpha-radiation.

We estimated the radionuclide concentrations of U, Th, and K using high-resolution low background gamma-ray spectrometry (Guibert and Schvoerer, 1991). The obtained concentrations were then turned into beta-dose rates using conversion factors after Guérin et al. (2011) and corrected using grain size attenuation factors following Guérin et al. (2012). The effect of water on dose rate was corrected after Nathan and Mauz (2008). We estimated the saturation water content based on the grain size distribution as suggested in Nelson and Rittenour (2015). The sample-specific percentages of the sand, silt, and clay fraction are displayed in Table S1 in the supplementary material. We have used the fraction of 0.5±0.2 (of the saturation value) as a representative value to approximate the past water content. We increased the obtained value to 20±8% for samples (Koz16 to Koz21) due to the mudflow origin of layer 11b downwards.

Gamma-dose rates were estimated using artificial dosimeters ($Al_2O_3$:C chips; see Kreutzer et al., 2018 for further details) for all samples. The chips were first heated up for 10 min at 350° C. Three chips were inserted in each aluminium tube and remained in the sediment for 271 days. After retrieving, the stored energy was measured using Daybreak 2200 OSL reader system (Bortolot, 2000). The chips were stimulated through green light (Nichia NSPG10) and the emissions were recorded through a 7.5 mm Hoya U-340 filter. For comparison, the gamma-dose rate was also estimated using radioelement concentrations derived from the gamma-ray spectrometry. The concentrations were converted to the dose rate after convention factors tabulated in (Guérin et al., 2011) and corrected for water content following (Guérin and Mercier, 2012).

The cosmic-dose rate was calculated using the coordinate of the site and the overburden depth after the procedure in Prescott and Hutton, 1994; Prescott and Stephan (1982). The uncertainty of the cosmic dose rate was estimated at 10% after Prescott and Hutton (1994).

The internal dose rate was estimated using K and Rb concentrations of 12.5±0.5% (Huntley and Baril, 1997) and 460±20 ppm after Mejdahl (1987) respectively. The internal dose rate for quartz coarse grains was taken from Mejdahl (1987).

**2.5 Luminescence signal measurements**

We applied several protocols to both quartz and feldspar grains and accordingly the corresponding signals were used for dating. We have measured blue-OSL and VSL for quartz grains. In addition, IRSL at 50°C, and $pIR_{50}IRSL_{290}$ at an elevated temperature (290 °C) were measured to establish ages based on feldspar grains. Nevertheless, this approach potentially could disclose the history of grains' bleaching, which is a worthy matter of consideration since the accuracy of the obtained ages heavily depends on it. Below, the setting for each protocol is explained.

**Blue optically stimulated luminescence (blue-OSL)**

We used the single aliquot regenerative (SAR) dose protocol (Murray and Wintle, 2000) to estimate the equivalent dose ($D_e$) for each sample.

First, the dominance of the fast-decaying signal favourable for relatively young sediment samples was tested. We simply compared the blue-OSL signal from one of Kozarnika's samples with calibrated quartz Risø batch 90 (Hansen et al., 2015), which is known to be dominated by the fast decaying luminescence signal. In addition, a linearly modulated OSL (LM-OSL, Bulur, 1996) technique was applied to deconvolute the signal components for this sample to be compared with the calibration quartz. $D_e$ estimation was carried out using Analyst

software v. 4.53 (Duller, 2015). A single saturating exponential function was used for fitting the dose-response curve.

The regenerative dose steps were followed by a null dose delivered to monitor charge transfers. This step was followed by a repetition of the first regenerative dose to verify significant sensitivity changes. In the end, the same dose as the first regenerative was delivered to the samples and the corresponding signal was measured after stimulating with IRSL followed with blue OSL to check any significant contamination by feldspar grains after Duller (2003).

The luminescence signal was measured at 125°C for 40 s after preheating at 260°C for 10 s. The preheat plateau test was applied to sample Koz2 to select an appropriate temperature before measuring the signal in SAR protocol (Murray and Wintle, 2000). In this test, $D_e$s were measured at various degrees starting from 200°C and reaching 300°C (ramping up by 20°C at each step). The cut heat was 40°C lower than the corresponding preheat temperature. Dose-recovery tests were conducted on some samples to monitor the reliability of the SAR protocol's parameters. Samples were bleached for 100 s using blue light, followed by a pause of 10,000 s. For the second time samples were bleached using blue light and then they received a beta dose inside the OSL reader approximately equivalent to their natural doses (Koz2, 4, 7, 10).

**Infrared stimulated luminescence ($IRSL_{50}$ and $pIR_{50}IRSL_{290}$)**

K-feldspars were used for estimating the $D_e$s for some of the samples to obtain independent ages, also revealing the grains' bleaching histories. Particularly, K-feldspar is favourable when the expected temporal range is higher than what the blue-OSL signal of quartz can achieve. Due to this higher upper age limit, this mineral has been used to unravel the temporal frameworks attributed to the Middle and also Lower Palaeolithic periods of the cave. Having said that, the drawback of using feldspar is athermal anomalous fading (loss of signal over time (Wintle, 1973)) that impedes the proper estimation of the true $D_e$. To overcome this problem, we determined the fading rate (Huntley and Lamothe, 2001) and corrected its effect on $D_e$. In this study, for three samples Koz4, Koz8, and Koz11, IRSL signals were measured (six aliquots for each sample) following fading measurement after a pause of approximately 1 h and 4 h. The fading rate was calculated using the function *Luminescence::analyse_FadingMeasurement()* implemented in the R (R Core Team, 2021) 'Luminescence' (Kreutzer et al., 2012; Kreutzer et al., 2021) package after methodological work by (Huntley, 2006). These values were then used to correct the $D_e$ estimates using *Luminescence::calc_Huntley2006()* after Kars et al., 2008 and King et al., 2018 also embedded in the R 'Luminescence' package. A single saturating exponential function was used to generate a dose-response curve.

Furthermore, we measured the IRSL signal at an elevated temperature following the IRSL at 50°C. This method was suggested after (Buylaert et al., 2011; Li and Li, 2011; Thiel et al., 2011; Thomsen et al., 2011, 2008) and it is proposed that the signals do not suffer from the fading, or at least the fading rate can be considered as insignificant (Buylaert et al., 2012, 2011). The parameters' setting for measuring this signal was derived from Buylaert et al., (2012) and was applied to a large number of samples containing 4 to 12 aliquots.

**Infrared radiofluorescence (IR-RF)**

Aside from the IRSL signal, K-feldspar emits another signal during ionising radiation, which is detected in the infrared wavelength range, known as IR-RF (for a recent review see Murari et al., 2021). The advantage of employing this signal is the larger age limit, which presumably could cover the temporal range attributed to the Lower Palaeolithic sequence of the cave. For IR-RF measurements, we have employed the parameters' setting suggested by Frouin et al. (2017). The regenerative signals were measured after bleaching of ca 3 h (10,800s). To ensure this time sufficiently reset the natural IR-RF signal, we also carried out a bleaching test.

The $D_e$s for samples Koz11, Koz14, Koz16, Koz18, Koz20, and Koz21 were estimated through the approach of horizontal and vertical sliding (Kreutzer et al., 2017; Murari et al., 2018) implemented in *Luminescence::analyse_IRSAR.RF()*.

**Violet stimulated luminescence (VSL)**

Unlike the relatively early saturation of the fast decaying blue-stimulated luminescence signal, some slow decaying components in quartz are deemed to be of higher saturation dose (Jain, 2009). This makes them attractive for dating older sediment like the Lower Palaeolithic sequences. Thus, we have applied the SAR protocol suggested by Ankjærgaard et al., (2016) to estimate the $D_e$ based on deep traps. This protocol was designed in a way that first the fast-decaying component is depleted using blue light stimulation and violet stimulation is then applied to probe the slow decaying signal with a higher saturation dose. We tested this technique on several samples (Koz8, 14, 16, 18, 21). However, the outcome of this application was not promising (all signals were in apparent saturation), therefore, we proceeded with the multiple aliquot additive dose (MAAD) protocol as an alternative solution to the standard SAR protocol offered in (Ankjærgaard et al., 2016). We used one of the youngest samples (Koz4) for which an independent age using the blue OSL technique was estimated and for which we had enough grains available to prepare a large number of aliquots.

The prepared samples were categorised into several fractions (each group comprising six aliquots) which were exposed to various amounts of beta irradiations on top of the natural dose. The first irradiative dose was set to 117 Gy and gradually it was increased to the dose of 2760

Gy. In the next step, following the approach of Ankjærgaard et al. (2016) we measured only the natural luminescence signal ($L_n$) which was corrected by the test dose signal ($T_n$) for each set of irradiated samples to minimise the impact of sensitivity change arising from repeated irritations and heating of the samples. Then the obtained L/T values were subsequently used to construct the MAAD dose-response curve fitted using a Lambert W function (Pagonis et al., 2020). Afterwards, the $L_n/T_n$ ratios measured from the natural samples were used (six aliquots for each natural sample) to estimate the $D_e$s (see result section).

## 3. Results

### 3.1 Dose rate

Table 2 shows the obtained concentrations of U, Th, and K. The equivalent U concentration was determined from the top (pre-$^{226}$Ra) and the bottom of the chain (post-$^{226}$Ra). This allows checking potential disequilibria in the U chain (Guibert et al., 2009). For samples Koz6, Koz7, Koz18, radioactive disequilibria were observed. To minimise this effect on the dose rates, instead of using the obtained values from the bottom of the chains (which were smaller than the top vaules), the average of the top and bottom concentrations was calculated and employed to estimate the dose rates for those samples (Table 3).

Table 2

The beta-dose rate for all samples ranged from 0.86±0.04 Gy/ka to 1.70±0.08 Gy/ka. The *in situ* and laboratory (i.e. from the concentrations of K, U and Th) gamma-dose rates ranged from 0.19± (<0.01) Gy/ka to 0.72±0.01 Gy/ka and from 0.49±0.02 Gy/ka to 0.97±0.03 Gy/ka, respectively. We have illustrated the two distinct series of gamma dose rates in Fig. 3. As shown in this figure, most *in situ* gamma-dose rates were significantly smaller than the corresponding gamma-dose rates obtained through means of gamma-ray spectrometry. It should be noted that we did not have a reliable estimation of the water content at sampling data, thus, it is likely that our estimation of the past water contents (varying between 14±6% to 20±8 %) is not in close alignment with the current water content. However, this does not explain the substantial discrepancies observed between the two dose rate results. It is more likely that the limestone pebbles and gravels that can readily identify in Fig. 2 caused a heterogeneous environment in which the *in situ* gamma dose rate values are smaller than the laboratory measurements. Therefore, we considered the *in situ* values more representative of the gamma dose rates received by the samples and used those values to determine the final dose rate. Particularly, because they cover gamma rays from larger distances and hence provide more

accurate estimates. The internal dose rate for quartz was set to 0.06±0.03 Gy/ka and a value of 0.90±0.14 Gy/ka was obtained for K-feldspar. Cosmic dose rates varied between 0.06±0.01 Gy/ka to 0.09±0.01 Gy/ka. In the end, the final dose rate for quartz and K-feldspar grains vary between 1.21±0.05 Gy/ka and 2.38±0.09 Gy/ka, and between 2.05±0.15 Gy/ka and 3.22±0.16 Gy/ka, respectively.

Table 3

Fig. 3.

### 3.2 Equivalent dose ($D_e$) determination

**Blue-OSL**

Fig. S2 in the supplementary material illustrates with pseudo-LM OSL (Bos and Wallinga, 2012) the presence of a fast-decaying signal at the beginning of the curve, but it also highlights at least contamination with another signal, at the end of the curve. Fig. S3 (true LM-OSL) revealed that presumably, the slow decaying signals (slow components) are also contributed to the luminescence signal.

We employed late background subtraction; the signal was measured using channels 1 to 3 (0.3 s) and the background was set to 300 to 399 (10 s). The recycling ratios, (a representative value for expressing the sensitivity change after administrating the cycles of heating and irradiating) were within 20% of the unity for all samples. Furthermore, the recuperation signal ratio following the received zero dose was less than 5%. An IR depletion ratio test Duller (2003) was carried out at the end of the SAR protocol and the results were within 10% for all samples. Fig. S4 in the supplementary material depicts the outcome of the preheat test for sample Koz2. We considered 260 ° C and 220° C as acceptable temperatures for the preheat and cut-heat in our SAR protocol; using such elevated temperatures allows subtracting a late background by removing less stable components than the fast component (Jain et al., 2003). Dose recovery ratios for samples Koz2, Koz4 (given dose ca 48 Gy), Koz7 and Koz10 (given dose ca 83 Gy) resulted in 1.02±0.04, 1.01±0.03, 0.96±0.08, 0.91± 0.07, respectively. These values are consistent with 1 within uncertainties and fulfil the standard criterion (commonly accepted is within 10% of unity), indicating the suitability of the SAR protocol's parameters for our samples. However, the smooth reduction in these values alongside increasing the $D_e$s, indicates that reaching the non-linear part of the dose-response curve and may give rise to $D_e$ underestimation.

Fig. 4a and Fig. 5a show typical dose-response curves, and a visual representation of the $D_e$ distribution for sample Koz4 as an example. We have estimated the central dose for each

sample using the arithmetic average (as suggested for multi-grain OSL by (Guérin et al., 2017)), and its uncertainty was determined through the standard error of the mean. The estimated central doses ranged from 48±2 Gy to 117±9 Gy for samples Koz1 to Koz10 (see Table 4). We also measured blue OSL signals for subsequent samples, however, since we reached the saturation limit of the signal, further results were considered untrustworthy or at least underestimated.

**$IRSL_{50}$ and $pIR_{50}IRSL_{290}$**

$IRSL_{50}$ signals for three samples were measured by integrating the first 6 s and subtracting the last 56 s as the background. The obtained *g*-values (measured for six aliquots per sample) for samples Koz4, Koz8 and Koz11 resulted in 3.25±0.04 (3.52±0.04, norm. 2 days) %/decade, 3.31±0.04 (3.58±0.04, norm. 2 days) %/decade, 3.35±0.07 (3.63±0.07, norm. 2 days) %/decade (see Fig S5). The fading corrected $D_e$s for these three samples were 109±1 Gy, 171±4 Gy, 512±72 Gy, respectively. The typical dose-response curves and $D_e$ distribution for sample Koz4 are illustrated in Fig. 4c and Fig. 5c, respectively.

The $pIR_{50}IRSL_{290}$ signals were measured using the first 8 s and the background was subtracted using the last 60 s of the shine-down curves. The recycling ratios were within 10% of unity and recuperation ratios were less than 5%. The dose-response curves and the $D_e$ distribution for sample Koz4 are depicted in Fig. 4b and Fig. 5b, respectively. The $D_e$ representing the central equivalent dose for all samples was determined using the arithmetic average of $D_e$ values and its uncertainty was estimated using the standard error of the mean. The obtained $D_e$s for our samples varied between 95±3 (Koz2) to 671±36 Gy (Koz14) (see Table 4). Due to the lack of K-feldspar grains for Koz15, we could not measure any signal, however, for the subsequent samples, the corresponding signals were mainly in or close to saturation and thus the outcome was not considered trustworthy.

Fig. 4.

Fig. 5.

**Infrared-radiofluorescence (IR-RF)**

The result of the bleaching test on sample Koz11 is displayed in Fig. S6. This figure shows that a bleaching time of 10,800 s appears to be sufficient, lying within the plateau. The IR-RF signal was measured using a channel resolution of 10 s. The observed scatter in the points after reaching the plateau is probably induced by negligible movement of grains on the sample

carrier. Typical IR-RF signals for samples Koz11, Koz18, Koz21 are shown in Fig. 6. The natural and regenerative signals are illustrated with red and green, respectively. The horizontal and vertical sliding method was successfully applied to natural signal and an excellent match between natural signal and regenerative is observed. The $D_e$ distributions for samples Koz11, Koz18, and Koz21 are represented in Fig. 7 using kernel density estimate (KDE) plot. The $D_e$ representing the central equivalent dose for each sample is estimated using the arithmetic average and its uncertainty was determined using the standard deviation.

Fig. 6.

Fig. 7.

**Violet stimulated luminescence (VSL)**

A typical dose-response curve alongside the natural and regenerative signals observed after applying the VSL (SAR) protocol is shown in Fig. S7 for one sample. Fig. S8 shows a smooth increase in the obtained $L_n/T_n$ values as samples' depths are increased along with the profile. This gradual rise suggested that VSL has the potential to yield chronological information, as was already observed in (Ankjærgaard et al., 2016). Fig. 8 illustrates the L/T distribution obtained for each set of six aliquots prepared originally from Koz4; while the first set corresponds to the natural dose, all other sets were irradiated in the laboratory with increasing doses on top of the natural. We tested several fitting functions on our data set. Finally, as depicted in Fig. 8, we fitted a dose-response curve using a Lambert W function to our dataset, which seems to be more justified than other commonly fitting dose-response curve functions (Pagonis et al., 2020). Subsequently, the $L_n/T_n$ obtained from the natural samples were projected onto the fitted curve (Fig. S9). Because of the nature of the MAAD approach, which adds doses on a natural sample that already has a dose, the dose-response curve necessarily intersects with the y-axis. Theoretically, one could attempt to estimate the equivalent dose for the first sample from the intersection of the curve with the x-axis. Due to the exponential character of the curve, this extrapolation comes at the cost of very large uncertainties; hence it was not used here. However, the $L_n/T_n$ signal of Koz4 project onto the MAAD dose-response curve should result in an equivalent dose around 0. We estimated a value of 11±12 Gy for this sample, which is consistent with the zero dose within uncertainty. To estimate the equivalent dose of all other samples, the natural equivalent dose of sample Koz4 based on quartz blue OSL was added to all estimated results to determine the final $D_e$ for each sample.

Fig. 8.

### 3.3 Age estimation

The obtained ages based on the various signals are presented in Table 4. The OSL dating for the uppermost sample (Koz1) belonging to layer 5a, exhibited an age of 32±2 ka (one sigma). Gradually, the OSL ages increase smoothly with depth until layer 10b (sample Koz11), for which two aliquots out of ten were in saturation. Thus, we considered this age (141±12 ka) to be a minimum age. The corresponding ages for samples Koz11 and Koz12 estimated based on $pIR_{50}IRSL_{290}$ signals led to 161±13 ka and 199±12 ka (one sigma). Subsequently, only the OSL age for layer 10a (59±4 ka) and younger samples above were considered reliable (Fig. 9).

As shown in Fig. 9 (inset) (between layer 5a to layer 10a), the $pIR_{50}IRSL_{290}$ ages were determined for a number of samples. Generally, at first glance, it can be concluded that the $pIR_{50}IRSL_{290}$ ages are older than the corresponding OSL ones. However, apart from one sample (Koz2 from layer 5b), for which no overlapping between the OSL and $pIR_{50}IRSL_{290}$ ages is observed within two sigma (26-33 ka for OSL and 35-43 ka for $pIR_{50}IRSL_{290}$), the rest overlap and the age outcome from the two approaches can be generally evaluated consistently.

The IRSL ages which were fading-corrected were estimated for three samples. All of them are older compared to both, OSL and $pIR_{50}IRSL_{290}$ ages. The obtained IRSL ages resulted in 45±3 ka and 66±4 ka, respectively, for samples Koz4 (layer 6/7) and Koz8 (layer 9c). At 95% confidence, these two ages exhibit timeframes of 39-51 ka and 58-75 ka that overall are in alignment with the periods of 33-41 ka and 48-74 ka ascertained from $pIR_{50}IRSL_{290}$. Nevertheless, the IRSL age of sample Koz11 (layer 10b) 250±40 ka is significantly larger than the corresponding $pIR_{50}IRSL_{290}$ age of 161±13 ka. The IR-RF age for this sample resulted in 201±17 ka; thus, it seems that the $pIR_{50}IRSL_{290}$ age for this sample could be underestimated. The $pIR_{50}IRSL_{290}$ ages increase in depth up to layer 10c. Afterwards, we have a clear indication of signal saturation (four aliquots out of six) for sample Koz16 (layer 11b). From this layer down to the lowermost layer, only IR-RF and VSL ages are available.

Besides the VSL ages for the oldest part of the sequence, several ages were also determined for the youngest samples. Although at first glance, the VSL ages for the subsequent samples Koz5, Koz6, and Koz7 do not seem consistent with the outcome of other dating techniques, their corresponding age intervals overlap one another (at two sigma).

Getting back to the older part of the sequence, we can see an excellent match between IR-RF- and VSL- based results, 279±29 ka and 324±94 ka, respectively for sample Koz14, layer 10c as an example. This picture does not hold for the older ages, however, still within two sigma,

both ages can be considered consistent, given the large error inherent for the VSL ages observed for all samples and related to the shape of the dose-response curve.

The IR-RF ages are more precise (i.e., they show smaller analytical error bars) and are less scattered. The VSL age estimated for the oldest sample Koz21 belonging to layer 13c in the profile was estimated at 704±168 ka. This age seems to be greater than the corresponding age based on IR-RF (387±28 ka), although the large uncertainty obtained for the VSL age, makes a reasonable comparison difficult.

Table 4

Fig. 9.

## 4. Discussion

### 4.1 How confident are we about the obtained chronologies?

In the previous section, we presented ages based on different luminescence dating techniques. Since the age discrepancies observed between the various signals were not always negligible, it is worthwhile to critically reflect the ages and discuss reasons for these differences.

The IRSL ages estimated for all three samples led to older ages compared to other results. King et al. (2018) argued that employing a single saturating exponential fit can result in overestimated $D_e$ dependent on the characteristic of the dose-response curve. Nevertheless, it should be noted that a single saturating exponential function perfectly described the dose-response curve for these three samples in this study. A general-order kinetic (GOK, Guralnik et al., 2015) also was tried for fitting sample Koz11 for which the $D_e$ was not located in the linear part of the dose-response curve, and hence varying fitting functions could potentially lead to different outcomes. Applying this fitting resulted in a larger value compared to the single-saturating exponential function.

It is worth mentioning that the GOK can result in more reliable estimation only if the higher part of the dose-response curve is thoroughly defined by incorporating relatively large regenerative points (King et al., 2018). The largest regenerative dose used for generating the dose-response curve for Koz11 was only 600 Gy, while the individual $D_e$ s of ca 600-700 Gy were obtained for this sample. This could justify why applying GOK resulted in a larger $D_e$, and thus it was not a suitable function for our dataset. Having said that, even if the shape of the dose-response curve is considered problematic for Koz11, for younger samples, Koz4 and Koz8 this is not the case. Therefore, we can argue that it is more likely that the obtained *g*-values are not displaying the true measures and they are possibly overestimated. The proper

543 estimation of the fading rate in percentage per decade (the *g*-value) is a challenging task and
544 minute variations in temperature and conditions can result in a very different estimate (cf.
545 Kadereit et al. (2020) and the related public discussion). Although the reason behind this is
546 not clear, it is likely that our estimation of the *g*-value, which is based on maximum pausing of
547 only 4 h, was insufficient to properly determine the fading rate in the laboratory.
548 Previously in section 3.3, it was stated that $pIR_{50}IRSL_{290}$ ages for the upper part of the sequence
549 seemed to be slightly older than the OSL ages. However, the $pIR_{50}IRSL_{290}$ signal may contain
550 a residual dose (hard to bleach signal, Buylaert et al., 2011) contributing to the measured signal
551 and giving rise to overestimated age. Due to the scarce amount of K-feldspar grains, we did
552 not measure residual dose for our samples, however, in the literature, the amount of 5-20 Gy
553 (e.g., Buylaert et al. 2011) was suggested as a reasonable measure. We calculated the residual
554 doses for the upper part of the sequence assuming that the OSL and $pIR_{50}IRSL_{290}$ ages agree
555 with one another. The values ranged from 9 Gy to 29 Gy, consistent with the values suggested
556 by Buylaert et al. (2011). Subtracting this range from the obtained $pIR_{50}IRSL_{290}$ $D_e$ resulted in
557 the ages in excellent accordance with the corresponding quartz OSL ages. Thus, the
558 discrepancies observed earlier between these two series of ages might be related to
559 'unbleachable' residual doses.
560 Furthermore, taking into account the slow beaching rate of the $pIR_{50}IRSL_{290}$ signal compared
561 to the OSL signal (Murray et al., 2012), we can safely conclude that the sediment samples were
562 well-bleached before burial. This inference is also supported from the sedimentological
563 perspective since the original nature of the sediments in the cave was identified as loess-
564 derivates and wind-blown loess (Muttoni et al., 2017). Although some scholars have argued
565 that these sediments should be categorised as loess-like and not (primary) loess (Jipa, 2014).
566 In addition, the bleaching rate of IR-RF is also considered similar to $pIR_{50}IRSL_{290}$ (Frouin et
567 al., 2017), hence the IR-RF ages do not suffer from an age overestimation as already observed
568 by an overall concordance between the $pIR_{50}IRSL_{290}$ and IR-RF ages.
569 The OSL and $pIR_{50}IRSL_{290}$ ages increase gradually along the profile until layer 10a.
570 Afterwards, due to the saturation, no OSL age was reported. Heydari and Guérin, (2018)
571 demonstrated that the Bayesian models implemented in BayLum (Guérin et al., 2021; Philippe
572 et al., 2019) can lead to a more accurate dose estimation when the signal is close or in
573 saturation, compared to 'classical analyses' using the Analyst software. Thus, in the future, it
574 might be worth applying Bayesian modelling on single grain measurements for samples older
575 than layer 10a and comparing the outcomes with other independent ages available based on
576 different signals.

The $pIR_{50}IRSL_{290}$ ages for layer 10b resulted in 161±13 ka (Koz11) and 199±12 ka (Koz12). The corresponding ages for sample Koz11 using IRSL, VSL and IR-RF yielded 250±40 ka, 321±77 ka, 201±17 ka, respectively, all older than $pIR_{50}IRSL_{290}$. Thus, the $pIR_{50}IRSL_{290}$ age for sample Koz11 appears to be underestimated. Albeit the first argument which immediately springs to mind is the possibility of fading, such conjecture was not derived from the rest of the samples, and it does not appear plausible here.

For the next layer (10b), the $pIR_{50}IRSL_{290}$ age (199±12 ka) with a $D_e$ of 416±16 Gy is in excellent accordance with the corresponding age using the IR-RF signal (201±17 ka). The same trend is observed for layer 10c where $pIR_{50}IRSL_{290}$ resulted in 281±19 ka whereas IR-IF exhibited 279±29 ka.

The $pIR_{50}IRSL_{290}$ ages estimated for layer 10c ($D_e$ of 659-671 Gy) were the oldest age obtained using this signal. Afterwards, for the lower layer (11b), measurements clearly show evidence for signal saturation (four aliquots out of six). On the other hand, IR-RF measurement for layer 11b resulted in $D_e$ of 888±23 Gy. Therefore, the interval between 671±36 Gy (the highest $D_e$ estimated based on $pIR_{50}IRSL_{290}$) and 888±23 Gy can be considered as a saturation level for the $pIR_{50}IRSL_{290}$ signal which is consistent with other findings (e.g., Yi et al., 2015). Although in the literature ca. 1,000 Gy was suggested as a threshold for IR-RF (Erfurt and Krbetschek, 2003), comparing this age with the VSL might imply that the signal saturation for IR-RF is around 923±23 Gy ($D_e$ of oldest sample in layer 13c). By looking at the chronological results from layer 11b to the lowermost layer (13c), it is not inconceivable to speculate that we already gradually reached a saturation level IR-RF signal at even above layer (11b) with the $D_e$ of 888±23 Gy. Comparing VSL ages determined for these layers with IR-RFs, could even reinforce this possibility although the large errors presented for VSL ages do not allow for a very precise and decisive conclusion.

More importantly, Muttoni et al. (2017) established a palaeomagnetism sequence for the Kozarnika cave suggesting the layer immediately after 13c lies in the Brunhes-Matuyama boundary with the timing of 780 ka. They also attributed layers 13a-c to layers L6 to L7 in the stratigraphical Danube loess-palaeosol presented in Marković et al. (2015) (their Fig. 16) and the link allows them to speculate that a period of 600-750 ka (early Brunhes) might represent the timeframe for layers 13a-c. Indeed, the silt fraction becomes more and more abundant from layers 11a to 13b, and the Kozarnika area is included in Pontic East European loess (domain V) (see Lehmkuhl et al., 2021). On the other hand, there is no loess near Kozarnika (see Evlogiev, 2007). The closest loess deposit is reported in distances from 60 km to 100 km of

610 the cave location. Furthermore, silt remobilized in the karst might be considered loess-like
611 (alluvial and aeolian), which extends more in the west than the loess (see for example Jipa,
612 2014 or the “lössartige und andere Lehme” of Fotakieva & Minkov, 1966). The sediment
613 accumulation of the lower layers of Kozarnika is endocarstic and therefore discontinuous, with
614 gaps posing difficulties to any quantification. Therefore, we cannot invalidate the hypothesis
615 of sedimentary lacks under the magnetic “event" at the lower part of layer 11b (around -6.50
616 m) as identified by Kovacheva et al. (in Guadelli et al., 2005) and Muttoni et al. (2017). This
617 might place the Brunhes-Matuyama limit at the base of layer 11b and not in layer 13, which is
618 in agreement with the macro-mammals assemblages of layer 11b (Guadelli et al., 2005, in
619 press; Fernandez and Crégut-Bonnoure, 2007; Sirakov et al., 2010).
620 In either way, this independent chronological data (palaeomagnetism sequence) can be seen as
621 a strong argument supporting the saturation assumption of IR-RF for layer 13. The VSL age of
622 704±168 ka for layer 13c, agrees with the period of 600-750 ka, however, only due to the very
623 large uncertainty. Apart from that, the agreement of the VSL ages with other independent ages
624 obtained for the Kozarnika sequence tends to confirm the overall accuracy of the VSL ages,
625 which is consistent with the observation of Ankjærgaard et al. (2016).
626 These large uncertainty margins, resulting from the leverage effect of the signal uncertainty
627 caused by the flat dose-response curve, are the main drawback of the VSL application.
628 However, this might be ameliorated by increasing the number of measured samples to specify
629 a more precise probability density distribution after projecting $L_n/T_n$s onto the dose-response
630 curve. This may lead to more confidence in the $D_e$ estimates in future studies.
631 **4.2 Unravelling the timing of humans in the cave**
632 The Kozarnika cave contains three main assemblages associated with the Lower, Middle, and
633 Upper Palaeolithic periods. For the Upper Palaeolithic sequence, some radiocarbon dates are
634 available (Guadelli et al., 2005, in press). Although some of these results were provided nearly
635 two decades ago (new procedures have been suggested since then for sample pre-treatments to
636 improve the accuracy and precision of radiocarbon dates e.g., Wood, 2015), comparing these
637 dates as independent ages with luminescence-based ages is still advantageous. The uppermost
638 luminescence-age based on OSL technique resulted in 32±2 ka for layer (5a), and 30±2 ka for
639 the layer below (layer 5b). The available radiocarbon age for layer 5b exhibited 31.2 ka cal.
640 BP (original data from Guadelli et al. (2005) and calibrated from Muttoni et al. (2017))
641 showing an excellent concordance with OSL ages within uncertainties. New radiocarbon ages

642 fall in the range of 29,219-30,030 ka cal. BP to 31,919-33,130 ka cal. BP for layer 5a and
643 36,152-37,276 ka cal. BP to 36,987-39,875 ka cal. BP for layer 5b (Guadelli et al., in press).
644 Following that, layer 5c represents the radiocarbon range of 40-44 ka cal. BP (original data
645 from Guadelli et al., (2005). These results agree with the new radiocarbon ages suggesting a
646 range of 39,998-41,592 ka cal. BP to 42,085-44,541 ka cal. BP (Guadelli et al., in press).
647 Although there is no luminescence age available for this layer, the age of the layer immediately
648 beneath (6/7) yielded 33±2 ka and 35±2 ka. Sequentially the radiocarbon dates for this layer
649 ranged from 42,194-45,025 ka cal. BP to 43,243-54,492 ka cal. BP (Guadelli et al., in press)
650 which is significantly older than the OSL ages.
651 The OSL ages for the Upper Palaeolithic assemblages (Kozarnikian) uncovered in layer 5a is
652 in good concordance with the radiocarbon age, however the discrepancies between the OSL
653 and radiocarbon ages for layers 5b and 5c (Guadelli et al. in press) are significant. One possible
654 scenario that could explain the discrepancies between the outcome of two distinct dating
655 methods could be the scatter between OSL $D_e$s for each sample (see Fig. 5a as an example). In
656 such a case implementing signal grain measurements which allows for properly applying a
657 broad body of statistical models could be preferable.
658 Layer 6/7 with OSL ages of 33±2 ka and 35±2 ka and radiocarbon age range of 42-54 ka cal.
659 BP was considered an intermediate level between the Middle and Upper Palaeolithic
660 (Kozarnikian) containing artefacts associated with both affinities. Still, this does not
661 necessarily imply the mixture of Middle and Upper affinities but rather a concatenation of
662 successive and/or alternately rapid occupations (see Guadelli et al., in press for more details).
663 Although such a situation seems infrequent, it has been already observed for example at
664 Mandrin cave (France) or at Buran Kaya III (Crimea) (Silmak et al., 2017).
665 The layer after 9ab is attributed to the termination of the Middle Palaeolithic period rendering
666 the Mousterian Levallois elements. The OSL age of 43±3 ka established for layer 9ab within
667 uncertainties agrees with the range of 41,030–39,260 ka cal. BP representing the termination
668 of the Mousterian industry after Higham et al. (2014). Heydari et al. (2020) used Bayesian
669 modelling specifically designed for treating OSL samples to reduce age uncertainties attributed
670 to Palaeolithic assemblages. In particular, they combined OSL ages with radiocarbon dates for
671 one Palaeolithic site and obtained chronologies that were more precise (Heydari et al., 2021).
672 Thus, applying Bayesian modelling to treat luminescence ages in combination with
673 radiocarbon dates seems advantageous in this context to improve the precision for the
674 continuous or discontinuous transition timeframe from the Middle to Upper Palaeolithic period.

675 A remarkable finding in layer 10b was a radius of an infant attributed to a Neanderthal, which
676 earlier was dated between 128 ± 13 ka and 183 ± 14 ka using OSL and $pIR_{50}IRSL_{290}$ techniques
677 (Tillier et al., 2017). Nevertheless, in the present study, we acknowledge that the OSL age of
678 128 ± 13 ka is underestimated, and we suggest an age of 201±17 ka, based on IR-RF, revealing
679 older deposit of the Neanderthal infant's skeleton. This result confirms the new
680 biochronological interpretation of the middle sequence of Kozarnika cave (Guadelli et al., in
681 press). Nevertheless, a stark contrast for the oldest layers exists between the biochronological
682 framework according to micromammals (Popov and Marinska, 2007) and the one based on
683 large mammal species (Guadelli et al., 2005; Fernandez and Crégut-Bonnoure, 2007; Sirakov
684 et al., 2010).
685 The Lower Palaeolithic industries were found from layer 11a downwards. The luminescence
686 dating suggested the onset of the Middle Palaeolithic period in the timeframe of 279±29 ka
687 (IR-RF) 324±94 ka (VSL), which is perfectly in line with what we expect from other
688 chronologies established for Middle Palaeolithic assemblages (Richter, 2011).
689 The youngest ages attributed to the Lower Palaeolithic assemblages in layer 11b were 337±23
690 ka (IR-RF), and 419±137 ka (VSL) and the oldest ages for layer 13c exhibited 387±28 ka (IR-
691 RF) and 704±168 ka (VSL). Although here luminescence dating is nearly at its age limit, taking
692 into account the smooth increase in the obtained ages along with the profile, does not seem to
693 support a period of 1,400-1,600 ka estimated using large mammal biochronology (Sirakov et
694 al., 2010) for layers 13a-c or even the revisited biochronological estimation of 1,200/1,000-
695 1,400/1,200 ka for the layer 12 to layers 13a-c suggested by Guadelli et al. (in press).
696 Surprisingly, the maximum age of 780 ka also questions the biochronology result for the Lower
697 Palaeolithic sequence of the Kozarnika cave (Brunhes-Matuyama boundary) proposed for layer
698 13c using palaeomagnetic dating (Muttoni et al., 2017). At this stage, it seems that further
699 chronological work is required to reach a decisive conclusion for the oldest layers of the
700 sequence.

701 **5. Conclusions**

702 A complete chronology for the Kozarnika cave was established using various luminescence-
703 dating techniques. Combining different approaches allowed us to successfully date sediments
704 from ca 30 ka to 700 ka unravelling the timing of human occupations during a large part of the
705 Palaeolithic. Nevertheless, at this stage, we cannot rule out the possibility of underestimated
706 timeframes for the layers containing the Lower Palaeolithic assemblages.

The obtained ages rely on the measurement of different signals for each sample to increase our confidence about the reliability of the outcomes. The overall accordance between the OSL with the $pIR_{50}IRSL_{290}$ ages for the upper part of the sequence makes it likely that both signals were completely bleached before mineral deposition. The same conclusion was deduced for the IR-RF signal, negating the possibility of age overestimation due to the slow beaching rate that often impedes the application of this method.

This study indicates that the saturation dose for the $pIR_{50}IRSL_{290}$ signal (at around 700 Gy to 900 Gy) led to ages of 291±22 ka and 281±19 ka as the oldest ages obtained in Kozarnika using this signal. On the other hand, the IR-RF saturated later, which enabled the age limit to be extended until 387±28 ka for this sequence. Moreover, the IR-RF doses measured on samples from layers 11a to 13c are indistinguishable, which probably indicates signal saturation. In that case, a dose of ~900 Gy might correspond to the field saturation limit of IR-RF for our samples. The IRSL ages were deemed to overestimate other ages presumably due to an inaccurate *g*-value estimate. Applying the VSL technique in combination with MAAD protocol resulted in ages that were consistent with other signal-based ages and implied the trustworthiness of outcomes. The drawback of this application was large uncertainty margins, which could be ameliorated by increasing the number of measured samples, and hence improving the precision. More crucially, Muttoni et al. (2017) assigned the Brunhes–Matuyama reversal (780 ka) to the layer beneath 13c using Palaeomagnetic dating. Subsequently, a timeframe of 600-750 ka was suggested for layers 13a-c (Muttoni et al., 2017) by correlating layers 13a-c to the Danube loess sequence layers L6-L7 (Marković et al., 2015). Thus, the obtained VSL age for layer 13c within error is consistent with that period. However, the large uncertainty on this VSL age renders a precise interpretation difficult. In addition, the independent age available for layers 13a-c (with the range of 600-750 ka) also might indicate that the IR-RF ages represent the minimum age for these layers.

Employing various luminescence signals in this study led to determining the timing of the human inhabitants of Kozarnika cave. The Kozarnikian assemblages discovered in layers 5a-c dates back to 32±2 ka and 33±2 ka. Generally, radiocarbon dates (Guadelli et al., 2005, in press) provided for Kozarnikian assemblages in layers 5a-c and 6/7 are older compared to luminescence dating.

This study revealed that the onset of the Middle Palaeolithic period happened at 279±29 ka (IR-RF) 324±94 ka (VSL) and it lasted until between 49±4 ka and 43±3 ka. The lower Palaeolithic assemblages in Kozarnika cave dated back to between 337±23 ka (IR-RF) and

704±168 ka (VSL). However, due to the supposed limit of luminescence dating in this dose range (setting our upper datable age limit), it is likely that they present minimum ages. Therefore, further chronological investigations using dating methods with extended age limit are required to shed light on the reliability of these ages and to further constrain the timing of the humans who lived during the Lower Palaeolithic period in the Kozarnika cave.

Table 1. Location of the sediment samples taken from the site.

| Sample name | Squares | X | Y | Z | Geological layers |
|---|---|---|---|---|---|
| Koz1 | H7 | 199.000 | 1498.900 | -4.259 | 5a |
| Koz2 | H7 | 199.000 | 1498.580 | -4.570 | 5b |
| Koz3 | H7 | 199.000 | 1498.333 | -4.609 | 5c |
| Koz4 | H6 | 199.000 | 1497.632 | -4.695 | 6/7 |
| Koz5 | H8 | 199.000 | 1499.560 | -4.549 | 6/7 |
| Koz6 | H8 | 199.000 | 1499.590 | -4.744 | 9ab |
| Koz7 | H7 | 199.000 | 1498.580 | -4.787 | 9ab |
| Koz8 | H7 | 199.000 | 1498.730 | -4.954 | 9c |
| Koz9 | H8 | 199.000 | 1499.560 | -4.896 | 9c |
| Koz10 | H7 | 199.000 | 1498.610 | -5.078 | 10a |
| Koz11 | F8 | 196.000 | 1499.119 | -5.232 | 10b |
| Koz12 | F7 | 196.000 | 1498.325 | -5.310 | 10b |
| Koz13 | H7 | 199.000 | 1498.770 | -5.259 | 10c |
| Koz14 | F8 | 196.000 | 1499.122 | -5.396 | 10c |
| Koz16 | F8 | 196.000 | 1499.107 | -5.880 | 11b |
| Koz18 | G11 | 197.419 | 1503.000 | -7.437 | 12 |
| Koz20 | G11 | 197.473 | 1503.000 | -7.551 | 13a |
| Koz21 | H11 | 198.000 | 1502.000 | -8.000 | 13c |

Table 2. The concentration of radionuclides obtained through gamma-ray spectrometry.

| Sample name | K (%) | U pre-$^{226}$Ra (ppm) | U post-$^{226}$Ra (ppm) | Th (ppm) |
|---|---|---|---|---|
| Koz1 | 1.58±0.02 | 1.93±0.08 | 1.97±0.02 | 6.83±0.07 |
| Koz2 | 1.48±0.02 | 1.17±0.07 | 1.24±0.02 | 4.75±0.05 |
| Koz3 | 1.54±0.02 | 1.19±0.07 | 0.99±0.02 | 4.95±0.06 |
| Koz4 | 1.47±0.02 | 1.13±0.07 | 1.33±0.02 | 5.26±0.06 |
| Koz5 | 1.44±0.02 | 1.11±0.07 | 1.29±0.02 | 4.72±0.06 |
| Koz6 | 2.15±0.02 | 2.08±0.08 | 1.64±0.02 | 7.92±0.07 |
| Koz7 | 2.06±0.02 | 1.92±0.07 | 1.55±0.02 | 7.63±0.06 |
| Koz8 | 1.41±0.02 | 1.14±0.05 | 1.32±0.01 | 4.84±0.05 |
| Koz9 | 1.37±0.02 | 1.24±0.07 | 1.13±0.02 | 4.78±0.05 |
| Koz10 | 1.35±0.02 | 1.21±0.07 | 1.17±0.02 | 4.95±0.05 |
| Koz11 | 1.13±0.01 | 0.88±0.06 | 0.89±0.01 | 4.08±0.05 |
| Koz12 | 1.20±0.01 | 0.92±0.06 | 0.91±0.01 | 4.30±0.05 |
| Koz13 | 1.29±0.02 | 1.16±0.07 | 1.11±0.01 | 5.64±0.05 |
| Koz14 | 1.34±0.01 | 1.25±0.05 | 1.17±0.01 | 5.75±0.05 |

| | | | | |
|---|---|---|---|---|
| Koz16 | 1.41±0.01 | 1.67±0.06 | 1.39±0.01 | 6.97±0.06 |
| Koz18 | 1.60±0.02 | 1.61±0.07 | 1.06±0.01 | 6.47±0.06 |
| Koz20 | 1.47±0.02 | 1.75±0.08 | 1.59±0.02 | 7.78±0.07 |
| Koz21 | 1.50±0.02 | 1.78±0.07 | 1.76±0.02 | 8.25±0.07 |

Table 3. The estimated dose rates for sediment samples in this study.

| Sample name | Water content (WF %) | Laboratory Gamma (Gy/ka) | *in situ* Gamma (Gy/ka) | Beta (Gy/ka) | Cosmic (Gy/ka) | Total $D_r$ Quartz (Gy/ka) | Total $D_r$ K-Feldspar (Gy/ka) |
|---|---|---|---|---|---|---|---|
| Koz1 | 15±6 | 0.81±0.03 | 0.31±0.02 | 1.31±0.06 | 0.09±0.01 | 1.77±0.07 | 2.61±0.15 |
| Koz2 | 14±6 | 0.63±0.02 | 0.34±0.01 | 1.13±0.06 | 0.09±0.01 | 1.62±0.06 | 2.45±0.15 |
| Koz3 | 14±5 | 0.63±0.02 | 0.39±0.02 | 1.17±0.06 | 0.09±0.01 | 1.70±0.07 | 2.54±0.15 |
| Koz4 | 15±6 | 0.66±0.02 | 0.31±0.02 | 1.14±0.06 | 0.09±0.01 | 1.60±0.07 | 2.44±0.15 |
| Koz5 | 14±5 | 0.63±0.02 | 0.38±0.01 | 1.12±0.05 | 0.09±0.01 | 1.65±0.06 | 2.48±0.15 |
| Koz6 | 14±5 | 0.97±0.03 | 0.54±0.01 | 1.70±0.08 | 0.09±0.01 | 2.38±0.09 | 3.22±0.16 |
| Koz7 | 15±6 | 0.92±0.03 | 0.59±0.01 | 1.61±0.08 | 0.09±0.01 | 2.34±0.09 | 3.18±0.16 |
| Koz8 | 14±5 | 0.63±0.02 | 0.50±0.00 | 1.11±0.05 | 0.09±0.01 | 1.75±0.06 | 2.59±0.15 |
| Koz9 | 14±6 | 0.60±0.02 | 0.39±0.00 | 1.06±0.05 | 0.09±0.01 | 1.60±0.06 | 2.44±0.15 |
| Koz10 | 15±6 | 0.60±0.02 | 0.33±0.01 | 1.05±0.05 | 0.09±0.01 | 1.53±0.06 | 2.36±0.15 |
| Koz11 | 15±6 | 0.49±0.02 | 0.20±0.00 | 0.86±0.04 | 0.09±0.01 | 1.21±0.05 | 2.05±0.15 |
| Koz12 | 15±6 | 0.52±0.02 | 0.19±0.00 | 0.92±0.05 | 0.09±0.01 | 1.25±0.06 | 2.09±0.15 |
| Koz13 | 14±5 | 0.62±0.02 | 0.25±0.01 | 1.03±0.05 | 0.08±0.01 | 1.43±0.06 | 2.26±0.15 |
| Koz14 | 14±6 | 0.64±0.02 | 0.35±0.00 | 1.06±0.05 | 0.08±0.01 | 1.56±0.06 | 2.39±0.15 |
| Koz16 | 20±8 | 0.68±0.03 | 0.57±0.01 | 1.09±0.07 | 0.08±0.01 | 1.80±0.07 | 2.64±0.15 |
| Koz18 | 20±8 | 0.70±0.03 | 0.72±0.01 | 1.19±0.08 | 0.07±0.01 | 2.04±0.08 | 2.87±0.16 |
| Koz20 | 20±8 | 0.74±0.03 | 0.50±0.03 | 1.16±0.07 | 0.07±0.01 | 1.79±0.08 | 2.62±0.16 |
| Koz21 | 20±8 | 0.78±0.04 | 0.23±0.01 | 1.20±0.07 | 0.06±0.01 | 1.55±0.08 | 2.39±0.16 |

Table 4. The $D_e$ and corresponding ages within uncertainties estimated using various luminescence signals.

| | OSL | | $pIR_{50}$-$IRSL_{290}$ | | IRSL | | VSL | | IR-RF | |
|---|---|---|---|---|---|---|---|---|---|---|
| Sample names | $D_e$ (Gy) | Age (ka) | $D_e$ (Gy) | Age (ka) | $D_e$ (Gy) | Age (ka) | $D_e$ (Gy) | Age (ka) | $D_e$ (Gy) | Age (ka) |
| Koz1 | 57±2 | 32±2 | | | | | | | | |
| Koz2 | 48±2 | 30±2 | 95±3 | 39±2 | | | | | | |
| Koz3 | 56±3 | 33±2 | | | | | | | | |
| Koz4 | 53±1 | 33±2 | 90±3 | 37±2 | 109±1 | 45±3 | | | | |
| Koz5 | 58±2 | 35±2 | | | | | | | | |
| Koz6 | 117±9 | 49±4 | 176±5 | 55±3 | | | 101±35 | 42±15 | | |
| Koz7 | 101±6 | 43±3 | 162±6 | 51±3 | | | 96±21 | 41±9 | | |
| Koz8 | 92±4 | 53±3 | 158±15 | 61±6 | 171±4 | 66±4 | 166±119 | 95±68 | | |
| Koz9 | 82±4 | 51±3 | 138±3 | 57±3 | | | | | | |
| Koz10 | 90±5 | 59±4 | 168±4 | 71±4 | | | | | | |

| | | | | | | | | |
|---|---|---|---|---|---|---|---|---|
| Koz11 | 330±22 | 161±13 | 512±72 | 250±40 | 390±91 | 321±77 | 411±18 | 201±17 |
| Koz12 | 416±16 | 199±12 | | | | | | |
| Koz13 | 659±39 | 291±22 | | | | | | |
| Koz14 | 671±36 | 281±19 | | | 504±144 | 324±94 | 668±56 | 279±29 |
| Koz16 | | | | | 755±245 | 419±137 | 888±23 | 337±23 |
| Koz18 | | | | | 768±227 | 377±113 | 835±20 | 290±18 |
| Koz20 | | | | | | | 906±17 | 346±23 |
| Koz21 | | | | | 1092±253 | 704±168 | 923±23 | 387±28 |

**Acknowledgements**

MH received funding from the GHKO association for her work in early 2016. The work was later supported by the LaScArBx. LaScArBx is a research programme supported by the ANR (ANR-10-LABX-52). Sebastian Kreutzer is thanked for providing the map and his support in analysing the IR-RF measurement data in 2016/2017.

Research in Kozarnika cave was undertaken within the framework of an international cooperation between the National Institute of Archaeology of the Bulgarian Academy of Sciences (N. Sirakov) and the UMR5199 CNRS PACEA (J.-L. Guadelli); the works of this Bulgarian-French cooperation are financially supported by the Advisory Committee of the Archaeological Research abroad of the French Ministry of Foreign Affairs (Mission Paléolithique de Bulgarie - dir. J.-L. Guadelli), by the CNRS (Centre National de la Recherche Scientifique), by the Region Aquitaine, by the University Bordeaux 1 (2004), by the Max Planck Institute for Evolutionary Anthropology, Department of Human Evolution (2004), ERC PALAEOCHRON (Dir. T. Higham) for 14C AMS dates (R. Hopkins, 2015-2018) and by the Bulgarian Academy of Sciences. To all of them, we send our deepest thanks.

**Author Contributions**

Conceptualization: Maryam Heydari, Guillaume Guérin, Jean-Luc Guadelli
Data curation: Maryam Heydari
Formal analysis: Maryam Heydari
Funding acquisition: Maryam Heydari, Jean-Luc Guadelli
Investigation: Maryam Heydari, Guillaume Guérin, Nikolay Sirakov, Philippe Fernandez, Catherine Ferrier, Aleta Guadelli, Jean-Claude Leblanc, Stanimira Taneva, Svoboda Sirakova, Jean-Luc Guadelli
Methodology: Maryam Heydari, Guillaume Guérin
Project administration: Jean-Luc Guadelli, Guillaume Guérin
Software: Maryam Heydari, Jean-Luc Guadelli
Supervision: Jean-Luc Guadelli, Guillaume Guérin
Visualization: Maryam Heydari, Jean-Luc Guadelli
Roles/Writing - original draft: Maryam Heydari
Writing - review & editing. Maryam Heydari, Jean-Luc Guadelli, Guillaume Guérin, Philippe Fernandez

**Figure captions**

Fig. 1. The Kozarnika cave is located in the northern hills of the Balkan Mountains, ca 30 km south of the Danube River, in the northwest of Bulgaria.

Fig. 2. Profile picture of the cave where sediment samples were taken from. The obtained luminescence ages according to different techniques are presented here.

Fig. 3. Comparison between the *in situ* and laboratory (gamma-ray spectrometry) gamma dose rate estimates. The *in situ* results are significantly lower compared to the laboratory measurements due to the heterogeneous environment observed in the sediment layers. Since limestone fragments from the bedrock are the source of radiation heterogeneities (limestone is generally poor in radioelements), this systematic discrepancy is expected. Thus, in situ measurements are more representative of the sediment burial conditions.

Fig. 4. Illustrating the dose-response curves for the OSL, $pIR_{50}IRSL_{290}$, and IRSL measurements derived from sample Koz4.

Fig. 5. $D_e$ distributions generated from OSL (A) $pIR_{50}IRSL_{290}$ (B) and $IRSL_{50}$ (C) measurements for sample Koz4 as an example using Abanico plot (Dietze et al., 2016).

Fig. 6. Typical IR-RF curves were obtained for three samples. Each plot represents results for one multiple grain aliquot. The natural signal is indicated by red-filled circles and the regenerated signal by green crosses. The horizontal and vertical sliding was used to estimate the $D_e$ for each subsample.

Fig. 7. The kernel density estimate (KDE) plots for three samples as examples to show typical $D_e$s distributions.

Fig. 8. VSL MAAD dose-response curve. The L/T s for each set of irradiated samples are shown in this figure. For the fitting, we applied a dose-response curve function based on the Lambert W function. The value of 11±12 Gy was obtained using this fitting for sample Koz4 (not irradiated), which within uncertainties is consistent with zero.

Fig. 9. The age-depth plot for all samples in this study covering the period of ca 30 ka to 700 ka using various luminescence signals. To provide better insight into the ages from Koz1 to Koz10 they are depicted in the inset.

852 **References**

853 Alex, B., Mihailović, D., Milošević, S., Boaretto, E., 2019. Radiocarbon chronology of Middle
854 and Upper Paleolithic sites in Serbia, Central Balkans. Journal of Archaeological
855 Science: Reports 25, 266–279. https://doi.org/10.1016/j.jasrep.2019.04.010
856 Ankjærgaard, C., Guralnik, B., Buylaert, J.-P., Reimann, T., Yi, S.W., Wallinga, J., 2016.
857 Violet stimulated luminescence dating of quartz from Luochuan (Chinese loess
858 plateau): Agreement with independent chronology up to ~600 ka. Quaternary
859 Geochronology 34, 33–46. https://doi.org/10.1016/j.quageo.2016.03.001
860 Ankjærgaard, C., Jain, M., Wallinga, J., 2013. Towards dating Quaternary sediments using the
861 quartz Violet Stimulated Luminescence (VSL) signal. Quaternary Geochronology 18,
862 99–109. https://doi.org/10.1016/j.quageo.2013.06.001
863 Bortolot, V.J., 2000. A new modular high capacity OSL reader system. Radiation
864 Measurements 32, 751–757. https://doi.org/10.1016/S1350-4487(00)00038-X
865 Bos, A.J.J., Wallinga, J., 2012. How to visualize quartz OSL signal components. Radiation
866 Measurements 47, 752–758. https://doi.org/10.1016/j.radmeas.2012.01.013
867 Bøtter-Jensen, L., Andersen, C.E., Duller, G.A.T., Murray, A.S., 2003. Developments in
868 radiation, stimulation and observation facilities in luminescence measurements.
869 Radiation Measurements 37, 535–541. https://doi.org/10.1016/S1350-4487(03)00020-
870 9
871 Bulur, E., 1996. An alternative technique for optically stimulated luminescence (OSL)
872 experiment. Radiation Measurements 26, 701–709. https://doi.org/10.1016/s1350-
873 4487(97)82884-3
874 Buylaert, J.-P., Jain, M., Murray, A.S., Thomsen, K.J., Thiel, C., Sohbati, R., 2012. A robust
875 feldspar luminescence dating method for Middle and Late Pleistocene sediments:
876 Feldspar luminescence dating of Middle and Late Pleistocene sediments. Boreas 41,
877 435–451. https://doi.org/10.1111/j.1502-3885.2012.00248.x
878 Buylaert, J.P., Thiel, C., Murray, A.S., Vandenberghe, D.A.G., Yi, S., Lu, H., 2011. IRSL and
879 post-IR IRSL residual doses recorded in modern dust samples from the Chinese Loess
880 Plateau. Geochronometria 38, 432–440. https://doi.org/10.2478/s13386-011-0047-0
881 Devièse, T., Karavanić, I., Comeskey, D., Kubiak, C., Korlević, P., Hajdinjak, M., Radović,
882 S., Procopio, N., Buckley, M., Pääbo, S., Higham, T., 2017. Direct dating of
883 Neanderthal remains from the site of Vindija Cave and implications for the Middle to
884 Upper Paleolithic transition. Proc Natl Acad Sci USA 114, 10606–10611.
885 https://doi.org/10.1073/pnas.1709235114
886 Dietze, M., Kreutzer, S., Burow, C., Fuchs, M.C., Fischer, M., Schmidt, C., 2016. The abanico
887 plot: Visualising chronometric data with individual standard errors. Quaternary
888 Geochronology 31, 12–18. https://doi.org/10.1016/j.quageo.2015.09.003
889 Doronichev, V.B., 2008. The Lower Paleolithic in Eastern Europe and the Caucasus: A
890 Reappraisal of the Data and New Approaches. PaleoAnthropology, 107–157.
891 Duller, G.A.T., 2015. The Analyst software package for luminescence data: overview and
892 recent improvements. Ancient TL 33, 35-42.
893 Duller, G.A.T., 2003. Distinguishing quartz and feldspar in single grain luminescence
894 measurements. Radiation Measurements 37, 161–165. https://doi.org/10.1016/S1350-
895 4487(02)00170-1
896 Erfurt, G., Krbetschek, M.R., 2003. IRSAR – A single-aliquot regenerative-dose dating
897 protocol applied to the infrared radiofluorescence (IR-RF) of coarse- grain K-feldspar.
898 Ancient TL 21, 35-42.
899 Evlogiev, Y. 2007. Evidence for the Aeolian origin of loess in the Danubian Plain. *Geologica*
900 *Balcanica* 36 (3-4), 31-39.

Fernandez, P., Crégut-Bonnoure, E., 2007. Les Caprinae (Rupicaprini, Ovibovini, Ovini et Caprini) de la séquence pléistocène de Kozarnika (Bulgarie du Nord): morphométrie, biochronologie et implications phylogéniques. *Revue de Paléobiologie* 26, 2, 425-503. http://halshs.archives-ouvertes.fr/halshs-00284574/en/

Ferrier, Leblanc, J.-Cl, Berthet, A.-L, Delfour, G, 2009. Kozarnika. Etude geologique et sedimentologique. Avalon, Sofia, pp. 13-27, In: Gatsov, I., Guadelli, J.-L. (Eds.), Saxa Loquuntur! "The stone will speak!".

Fewlass, H., Talamo, S., Wacker, L., Kromer, B., Tuna, T., Fagault, Y., Bard, E., McPherron, S.P., Aldeias, V., Maria, R., Martisius, N.L., Paskulin, L., Rezek, Z., Sinet-Mathiot, V., Sirakova, S., Smith, G.M., Spasov, R., Welker, F., Sirakov, N., Tsanova, T., Hublin, J.-J., 2020. A 14C chronology for the Middle to Upper Palaeolithic transition at Bacho Kiro Cave, Bulgaria. Nat Ecol Evol 4, 794–801. https://doi.org/10.1038/s41559-020-1136-3

Fotakieva, E.M., Minkov, M. 1966. Der Löß in Bulgarien. Eiszeitalter und Gegenwart. Band 17, 87-96, 3 abb., 1 tab.

Frouin, M., Huot, S., Kreutzer, S., Lahaye, C., Lamothe, M., Philippe, A., Mercier, N., 2017. An improved radiofluorescence single-aliquot regenerative dose protocol for K-feldspars. Quaternary Geochronology 38, 13–24. https://doi.org/10.1016/j.quageo.2016.11.004

Fu, Q., Hajdinjak, M., Moldovan, O.T., Constantin, S., Mallick, S., Skoglund, P., Patterson, N., Rohland, N., Lazaridis, I., Nickel, B., Viola, B., Prüfer, K., Meyer, M., Kelso, J., Reich, D., Pääbo, S., 2015. An early modern human from Romania with a recent Neanderthal ancestor. Nature 524, 216–219. https://doi.org/10.1038/nature14558

Galanidou, N., 2004. Early Hominids in the Balkans, in: Griffiths, H.I., Kryštufek, B., Reed, J.M. (Eds.), Balkan Biodiversity. Springer Netherlands, Dordrecht, pp. 147–165. https://doi.org/10.1007/978-1-4020-2854-0_9

Glen, E., Kaczanowski, K., 1982. Human remains. In: Excavation in the Bacho Kiro Cave (Bulgaria). Final Report. J. Kozlowski (ed.). Panstwowe Wydawnictwo Naukowe, Warszawa 75–79.

Guadelli, J.L., Sirakov, N., Ivanova, S., Sirakova, S., Anastassova, E., Courtaud, P., Dimitrova, I., Djabarska, N., Fernandez, P., Ferrier, C., Fontugne, M., Gambier, D., Guadelli, A., Iordanova, D., Iordanova, N., Kovatcheva, M., Krumov, I., Leblanc, J.C., Mallye, J.B., Marinska, M., Miteva, V., Popov, V., Spasov, R., Taneva, S., Tisterat-Laborde, N., Tsanova, T., 2005. Une séquence du Paléolithique inferieur au Paléolithique récent dans les balkans : La grotte kozarnika à oreshets (nord-ouest de la bulgarie), in: Molines, N, Moncel, M.H., undefined, Monnier, J.L. (Eds.), Les Premiers Peuplements En Europe. BAR, pp. 87–103.

Guadelli, J.-L., Sirakov, N., Delpech F., Dimitrova, I., Fernandez, P., Ferrier, C., Guadelli, A., Krumov, I., Leblanc, J.-Cl., Sirakova, S., Taneva, S., Tillier A.-m. In press. Earliest dispersals and migrations to Europe via the Balkans in Lower to Upper Palaeolithic: Evidence from Kozarnika Cave (Northern Bulgaria). *Symposium : Évolution de la biodiversité depuis plus d'un million d'années et rapports entre l'Homme et son environnement sur le littoral méditerranéen*. Nice 01-02 octobre 2020. 64p., 28 fig., 20 tab.

Guérin, G., Christophe, C., Philippe, A., Murray, A.S., Thomsen, K.J., Tribolo, C., Urbanova, P., Jain, M., Guibert, P., Mercier, N., Kreutzer, S., Lahaye, C., 2017. Absorbed dose, equivalent dose, measured dose rates, and implications for OSL age estimates: Introducing the Average Dose Model. Quaternary Geochronology 41, 163–173. https://doi.org/10.1016/j.quageo.2017.04.002

951 Guérin, G., Lahaye, C., Heydari, M., Autzen, M., Buylaert, J.-P., Guibert, P., Jain, M.,
952 Kreutzer, S., Lebrun, B., Murray, A.S., Thomsen, K.J., Urbanova, P., Philippe, A.,
953 2021. Towards an improvement of optically stimulated luminescence (OSL) age
954 uncertainties: modelling OSL ages with systematic errors, stratigraphic constraints and
955 radiocarbon ages using the R package BayLum. Geochronology 3, 229–245.
956 https://doi.org/10.5194/gchron-3-229-2021
957 Guérin, G., Mercier, N., 2012. Preliminary insight into dose deposition processes in
958 sedimentary media on a scale of single grains: Monte Carlo modelling of the effect of
959 water on the gamma dose rate. Radiation Measurements 47, 541–547.
960 https://doi.org/10.1016/j.radmeas.2012.05.004
961 Guérin, G., Mercier, N., Adamiec, G., 2011. Dose-rate conversion factors: update. Ancient TL
962 29, 5–8.
963 Guérin, G., Mercier, N., Nathan, R., Adamiec, G., Lefrais, Y., 2012. On the use of the infinite
964 matrix assumption and associated concepts: A critical review. Radiation Measurements
965 47, 778–785. https://doi.org/10.1016/j.radmeas.2012.04.004
966 Guibert, P., Lahaye, C., Bechtel, F., 2009. The importance of U-series disequilibrium of
967 sediments in luminescence dating: A case study at the Roc de Marsal Cave (Dordogne,
968 France). Radiation Measurements 44, 223–231.
969 https://doi.org/10.1016/j.radmeas.2009.03.024
970 Guibert, P., Schvoerer, M., 1991. TL dating: Low background gamma spectrometry as a tool
971 for the determination of the annual dose. International Journal of Radiation
972 Applications and Instrumentation. Part D. Nuclear Tracks and Radiation Measurements
973 18, 231–238. https://doi.org/10.1016/1359-0189(91)90117-Z
974 Guralnik, B., Jain, M., Herman, F., Ankjærgaard, C., Murray, A.S., Valla, P.G., Preusser, F.,
975 King, G.E., Chen, R., Lowick, S.E., Kook, M., Rhodes, E.J., 2015. OSL-
976 thermochronometry of feldspar from the KTB borehole, Germany. Earth and Planetary
977 Science Letters 423, 232–243. https://doi.org/10.1016/j.epsl.2015.04.032
978 Hajdinjak, M., Mafessoni, F., Skov, L., Vernot, B., Hübner, A., Fu, Q., Essel, E., Nagel, S.,
979 Nickel, B., Richter, J., Moldovan, O.T., Constantin, S., Endarova, E., Zahariev, N.,
980 Spasov, R., Welker, F., Smith, G.M., Sinet-Mathiot, V., Paskulin, L., Fewlass, H.,
981 Talamo, S., Rezek, Z., Sirakova, S., Sirakov, N., McPherron, S.P., Tsanova, T., Hublin,
982 J.-J., Peter, B.M., Meyer, M., Skoglund, P., Kelso, J., Pääbo, S., 2021. Initial Upper
983 Palaeolithic humans in Europe had recent Neanderthal ancestry. Nature 592, 253–257.
984 https://doi.org/10.1038/s41586-021-03335-3
985 Hansen, V., Murray, A., Buylaert, J.-P., Yeo, E.-Y., Thomsen, K., 2015. A new irradiated
986 quartz for beta source calibration. Radiation Measurements 81, 123–127.
987 https://doi.org/10.1016/j.radmeas.2015.02.017
988 Heydari, M., Guérin, G., 2018. OSL signal saturation and dose rate variability: Investigating
989 the behaviour of different statistical models. Radiation Measurements 120, 96–103.
990 https://doi.org/10.1016/j.radmeas.2018.05.005
991 Heydari, M., Guérin, G., Kreutzer, S., Jamet, G., Kharazian, M.A., Hashemi, M., Nasab, H.V.,
992 Berillon, G., 2020. Do Bayesian methods lead to more precise chronologies? 'BayLum'
993 and a first OSL-based chronology for the Palaeolithic open-air site of Mirak (Iran).
994 Quaternary Geochronology 59, 101082. https://doi.org/10.1016/j.quageo.2020.101082
995 Heydari, M., Guérin, G., Zeidi, M., Conard, N.J., 2021. Bayesian luminescence dating at Ghār-
996 e Boof, Iran, provides a new chronology for Middle and Upper Paleolithic in the
997 southern Zagros. Journal of Human Evolution 151, 102926.
998 https://doi.org/10.1016/j.jhevol.2020.102926
999 Higham, T., Douka, K., Wood, R., Ramsey, C.B., Brock, F., Basell, L., Camps, M.,
1000 Arrizabalaga, A., Baena, J., Barroso-Ruíz, C., Bergman, C., Boitard, C., Boscato, P.,

1001 Caparrós, M., Conard, N.J., Draily, C., Froment, A., Galván, B., Gambassini, P.,
1002 Garcia-Moreno, A., Grimaldi, S., Haesaerts, P., Holt, B., Iriarte-Chiapusso, M.-J.,
1003 Jelinek, A., Jordá Pardo, J.F., Maíllo-Fernández, J.-M., Marom, A., Maroto, J.,
1004 Menéndez, M., Metz, L., Morin, E., Moroni, A., Negrino, F., Panagopoulou, E.,
1005 Peresani, M., Pirson, S., de la Rasilla, M., Riel-Salvatore, J., Ronchitelli, A.,
1006 Santamaria, D., Semal, P., Slimak, L., Soler, J., Soler, N., Villaluenga, A., Pinhasi, R.,
1007 Jacobi, R., 2014. The timing and spatiotemporal patterning of Neanderthal
1008 disappearance. Nature 512, 306–309. https://doi.org/10.1038/nature13621
1009 Higham, T., Ramsey, C.B., Karavanic, I., Smith, F.H., Trinkaus, E., 2006. Revised direct
1010 radiocarbon dating of the Vindija G1 Upper Paleolithic Neandertals. PNAS 103(3),
1011 553-557.
1012 Hoffecker, J.F., 2009. The spread of modern humans in Europe. Proceedings of the National
1013 Academy of Sciences 106, 16040–16045. https://doi.org/10.1073/pnas.0903446106
1014 Hublin, J.-J., Sirakov, N., Aldeias, V., Bailey, S., Bard, E., Delvigne, V., Endarova, E., Fagault,
1015 Y., Fewlass, H., Hajdinjak, M., Kromer, B., Krumov, I., Marreiros, J., Martisius, N.L.,
1016 Paskulin, L., Sinet-Mathiot, V., Meyer, M., Pääbo, S., Popov, V., Rezek, Z., Sirakova,
1017 S., Skinner, M.M., Smith, G.M., Spasov, R., Talamo, S., Tuna, T., Wacker, L., Welker,
1018 F., Wilcke, A., Zahariev, N., McPherron, S.P., Tsanova, T., 2020. Initial Upper
1019 Palaeolithic Homo sapiens from Bacho Kiro Cave, Bulgaria. Nature 581, 299–302.
1020 https://doi.org/10.1038/s41586-020-2259-z
1021 Huntley, D.I., Baril, M., 1997. The K content of the K-feldspars being measured in optical
1022 dating or in thermoluminescence dating. Ancient TL 15, 11–13.
1023 Huntley, D.J., 2006. An explanation of the power-law decay of luminescence. J. Phys.:
1024 Condens. Matter 18, 1359–1365. https://doi.org/10.1088/0953-8984/18/4/020
1025 Huntley, D.J., Godfrey-Smith, D.I., Thewalt, M.L.W., 1985. Optical dating of sediments.
1026 Nature 313, 105–107. https://doi.org/10.1038/313105a0
1027 Huntley, D.J., Lamothe, M., 2001. Ubiquity of anomalous fading in K-feldspars and the
1028 measurement and correction for it in optical dating. Canadian Journal of Earth Sciences
1029 38, 1093–1106
1030 Hütt, G., Jaek, I., Tchonka, J., 1988. Optical dating: K-feldspars optical response stimulation
1031 spectra. Quaternary Science Reviews 7, 381–385. https://doi.org/10.1016/0277-
1032 3791(88)90033-9
1033 Jain, M., 2009. Extending the dose range: Probing deep traps in quartz with 3.06eV photons.
1034 Radiation Measurements 44, 445–452. https://doi.org/10.1016/j.radmeas.2009.03.011
1035 Jain, M., Murray, A.S., Bøtter-Jensen, L., 2003. Characterisation of blue-light stimulated
1036 luminescence components in different quartz samples: implications for dose
1037 measurement. Radiation Measurements 37, 441–449. https://doi.org/10.1016/S1350-
1038 4487(03)00052-0
1039 Jipa, D.C., 2014. The loess-like deposits in the Lower Danube basin. Genetic signif- icance.
1040 Geo-Eco-Marina 20, 7–18.
1041 Kadereit, A., Kreutzer, S., Schmidt, C., DeWitt, R., 2020. A closer look at IRSL SAR fading
1042 data and their implication for luminescence dating. Geochronology Discussions 2020,
1043 1–30. https://doi.org/10.5194/gchron-2020-3
1044 Kars, R.H., Wallinga, J., Cohen, K.M., 2008. A new approach towards anomalous fading
1045 correction for feldspar IRSL dating — tests on samples in field saturation. Radiation
1046 Measurements 43, 786–790. https://doi.org/10.1016/j.radmeas.2008.01.021
1047 King, G.E., Burow, C., Roberts, H.M., Pearce, N.J.G., 2018. Age determination using feldspar:
1048 Evaluating fading-correction model performance. Radiation Measurements 119, 58–
1049 73. https://doi.org/10.1016/j.radmeas.2018.07.013

1050 Kreutzer, S., Burow, C., Dietze, M., Fuchs, M.C., Schmidt, C., Fischer, M., Friedrich, J.,
1051 Mercier, N., Smedley, R.K., Christophe, C., Zink, A., Durcan, J., King, G.E., Philippe,
1052 A., Guérin, G., Riedesel, S., Autzen, M., Guibert, P., Mittelstrass, D., Gray, H.J., 2021.
1053 Luminescence: Comprehensive Luminescence Dating Data Analysis. Zenodo.
1054 https://doi.org/10.5281/zenodo.4729933
1055 Kreutzer, S., Martin, L., Guérin, G., Tribolo, C., Selva, P., Mercier, N., 2018. Environmental
1056 dose rate determination using a passive dosimeter: Techniques and workflow for α-
1057 Al2O3:C chips. Geochronometria 45, 56–67. https://doi.org/10.1515/geochr-2015-
1058 0086
1059 Kreutzer, S., Murari, M., Frouin, M., Fuchs, M., Mercier, N., 2017. Always remain suspicious:
1060 a case study on tracking down a technical artefact while measuring IR-RF. Ancient TL
1061 35, 20–30.
1062 Kreutzer, S., Schmidt, C., Fuchs, Margret, Dietze, M., Fischer, M., Fuchs, Markus, 2012.
1063 Introducing an R package for luminescence dating analysis Ancient TL 30, 1–8
1064 Lehmkuhl, F., Nett, J.J., Pötter, S., Schulte, P., Sprafke, T., Jary, Z., Antoine, P., Wacha, L.,
1065 Wolf, D., Zerboni, A., Hosek, J.,Markovic, S.B., Obreht, I., Sümegi, P., Veres, D.,
1066 Zeeden, C., Boemke, B., Schaubert, V., Viehweger, J., Hambach, U. 2021. Loess
1067 landscapes of Europe – Mapping, geomorphology, and zonal differentiation. *Earth-*
1068 *Science Reviews*. 215 (2021), 42p., 21 fig., 1 tab.
1069 http://dx.doi.org/10.1016/j.earscirev.2020.103496
1070 Li, B., Li, S.-H., 2011. Luminescence dating of K-feldspar from sediments: A protocol without
1071 anomalous fading correction. Quaternary Geochronology 6, 468–479.
1072 https://doi.org/10.1016/j.quageo.2011.05.001
1073 Marković, S.B., Stevens, T., Kukla, G.J., Hambach, U., Fitzsimmons, K.E., Gibbard, P.,
1074 Buggle, B., Zech, M., Guo, Z., Hao, Q., Wu, H., O'Hara Dhand, K., Smalley, I.J.,
1075 Újvári, G., Sümegi, P., Timar-Gabor, A., Veres, D., Sirocko, F., Vasiljević, D.A., Jary,
1076 Z., Svensson, A., Jović, V., Lehmkuhl, F., Kovács, J., Svirčev, Z., 2015. Danube loess
1077 stratigraphy — Towards a pan-European loess stratigraphic model. Earth-Science
1078 Reviews 148, 228–258. https://doi.org/10.1016/j.earscirev.2015.06.005
1079 Mejdahl, V, 1987. Internal radioactivity in quartz and feldspar grains. Ancient TL 5, 10–17.
1080 Murari, M.K., Kreutzer, S., Fuchs, M., 2018. Further investigations on IR-RF: Dose recovery
1081 and correction. Radiation Measurements 120, 110–119.
1082 https://doi.org/10.1016/j.radmeas.2018.04.017
1083 Murari, M.K., Kreutzer, S., King, G., Frouin, M., Tsukamoto, S., Schmidt, C., Lauer, T.,
1084 Klasen, N., Richter, D., Friedrich, J., Mercier, N., Fuchs, M., 2021. Infrared
1085 radiofluorescence (IR-RF) dating: A review. Quaternary Geochronology 64, 101155.
1086 https://doi.org/10.1016/j.quageo.2021.101155
1087 Murray, A.S., Thomsen, K.J., Masuda, N., Buylaert, J.P., Jain, M., 2012. Identifying well-
1088 bleached quartz using the different bleaching rates of quartz and feldspar luminescence
1089 signals. Radiation Measurements 47, 688–695.
1090 https://doi.org/10.1016/j.radmeas.2012.05.006
1091 Murray, A.S., Wintle, A.G., 2000. Luminescence dating of quartz using an improved single-
1092 aliquot regenerative-dose protocol. Radiation Measurements 32, 57–73.
1093 https://doi.org/10.1016/S1350-4487(99)00253-X
1094 Muttoni, G., Sirakov, N., Guadelli, J.-L., Kent, D.V., Scardia, G., Monesi, E., Zerboni, A.,
1095 Ferrara, E., 2017. An early Brunhes (<0.78 Ma) age for the Lower Paleolithic tool-
1096 bearing Kozarnika cave sediments, Bulgaria. Quaternary Science Reviews 178, 1–13.
1097 Nathan, R.P., Mauz, B., 2008. On the dose-rate estimate of carbonate-rich sediments for
1098 trapped charge dating. Radiation Measurements 43, 14–25.
1099 https://doi.org/10.1016/j.radmeas.2007.12.012

1100 Nelson, M.S., Rittenour, T.M., 2015. Using grain-size characteristics to model soil water
1101 content: Application to dose-rate calculation for luminescence dating. Radiation
1102 Measurements 81, 142–149. https://doi.org/10.1016/j.radmeas.2015.02.016
1103 Pagonis, V., Kitis, G., Chen, R., 2020. A new analytical equation for the dose response of
1104 dosimetric materials, based on the Lambert W function. Journal of Luminescence 225,
1105 117333. https://doi.org/10.1016/j.jlumin.2020.117333
1106 Philippe, A., Guérin, G., Kreutzer, S., 2019. BayLum - An R package for Bayesian analysis of
1107 OSL ages: An introduction. Quaternary Geochronology 49, 16–24.
1108 https://doi.org/10.1016/j.quageo.2018.05.009
1109 Popov, V.V., Marinska, M., 2007. An almost one million year long (Early to Late Pleistocene)
1110 small mammal succession from the archaeological layers of Kozarnika Cave in
1111 Northern Bulgaria. Courier Forschungsinstitut Senckenberg 259, 1, 79–92.
1112 Popov (Попов), 1933. The Mirizlivka cave. Contribution to the diluvial fauna and the culture
1113 of the diluvial man in Bulgaria.Попов, Р., 1933. Пещерата Миризливка. Приносъ
1114 къмъ дилувиалната фауна и културата на дилувиалния човекъ въ България.
1115 National Archaeological Museum (Sofia, Bulgaria) Издания на народния
1116 археологически музей. 26, 5–69.
1117 Prescott, J.R., Hutton, J.T., 1994. Cosmic ray contributions to dose rates for luminescence and
1118 ESR dating: Large depths and long-term time variations. Radiation Measurements 23,
1119 497–500. https://doi.org/10.1016/1350-4487(94)90086-8
1120 Prescott, J.R., Stephan, L.G., 1982. The contribution of cosmic radiation to the environmental
1121 dose for thermoluminescence dating. Latitude, altitude and depth dependences. Journal
1122 of the European Study Group on Physical, Chemical and Mathematical Techniques
1123 Applied to Archaeology (PACT) 6, 17–25.
1124 Preusser, F., Degering, D., Fuchs, M., Hilgers, A., Kadereit, A., Klasen, N., Krbetschek, M.,
1125 Richter, D., Spencer, J.Q.G., 2008. Luminescence dating: basics, methods and
1126 applications. E&G Quaternary Sci. J. 57, 95–149. https://doi.org/10.3285/eg.57.1-
1127 2.5
1128 R Core Team, 2021. R: A language and environment for statistical computing.
1129 Richter, D., Richter, A., Dornich, K., 2015. Lexsyg smart — a luminescence detection system
1130 for dosimetry, material research and dating application. Geochronometria 42, 202–209.
1131 https://doi.org/10.1515/geochr-2015-0022
1132 Richter, D., Richter, A., Dornich, K., 2013. lexsyg — a new system for luminescence research.
1133 Geochronometria 40, 220–228. https://doi.org/10.2478/s13386-013-0110-0
1134 Richter, J., 2011. When Did the Middle Paleolithic Begin?, in: Conard, N.J., Richter, J. (Eds.),
1135 Neanderthal Lifeways, Subsistence and Technology, Vertebrate Paleobiology and
1136 Paleoanthropology. Springer Netherlands, Dordrecht, pp. 7–14.
1137 https://doi.org/10.1007/978-94-007-0415-2_2
1138 Sirakov, N., Tsanova, T., Sirakova, S., Taneva, S., Krumov, I., Dimitrova I., Kovatcheva, N.,
1139 2007. Un nouveau faciès lamellaire du début du Paléolithique supérieur dans les
1140 Balkans. Paleo 19, 131–144. https://doi.org/10.4000/paleo.565
1141 Sirakov, N., Guadelli, J.-L., Ivanova, S., Sirakova, S., Boudadi-Maligne, M., Dimitrova, I., Ph,
1142 F., Ferrier, C., Guadelli, A., Iordanova, D., Iordanova, N., Kovatcheva, M., Krumov,
1143 I., Leblanc, J.-Cl., Miteva, V., Popov, V., Spassov, R., Taneva, S., Tsanova, T., 2010.
1144 An ancient continuous human presence in the Balkans and the beginnings of human
1145 settlement in western Eurasia: A Lower Pleistocene example of the Lower Palaeolithic
1146 levels in Kozarnika cave (North-western Bulgaria). Quaternary International 223–224,
1147 94–106. https://doi.org/10.1016/j.quaint.2010.02.023
1148 Slimak, L., Metz , L., Teyssandier, N., 2017. De la fin du Paléolithique moyen aux prémices
1149 du Paléolithique supérieur, pénombres et éclairages européens. Le troisième Homme.

Préhistoire de l'Altaï. J.J. Cleyet−Merle, M.V. Shunkov, J.M. Geneste, A.P. Derevianko, L. Slimak, A.L. Krivoshapkin, B. Gravina, A. Turq, B. Maureille eds. Éditions de la Réunion des musées nationaux – Grand Palais, pp. 125–133, 5 fig.

Strait, D.S., Orr, C.M., Hodgkins, J., Spassov, N., Gurova, M., Miller, C., Tzankov, T., 2016. The Human Fossil Record of Bulgaria and the Formulation of Biogeographic Hypotheses, in: Harvati, K., Roksandic, M. (Eds.), Paleoanthropology of the Balkans and Anatolia, Vertebrate Paleobiology and Paleoanthropology. Springer Netherlands, Dordrecht, pp. 69–78. https://doi.org/10.1007/978-94-024-0874-4_5

Thiel, C., Buylaert, J.-P., Murray, A., Terhorst, B., Hofer, I., Tsukamoto, S., Frechen, M., 2011. Luminescence dating of the Stratzing loess profile (Austria) – Testing the potential of an elevated temperature post-IR IRSL protocol. Quaternary International 234, 23–31. https://doi.org/10.1016/j.quaint.2010.05.018

Thomsen, K., Murray, A., Jain, M., 2011. Stability of IRSL signals from sedimentary K-feldspar samples. Geochronometria 38, 1–13. https://doi.org/10.2478/s13386-011-0003-z

Thomsen, K.J., Murray, A.S., Jain, M., Bøtter-Jensen, L., 2008. Laboratory fading rates of various luminescence signals from feldspar-rich sediment extracts. Radiation Measurements 43, 1474–1486. https://doi.org/10.1016/j.radmeas.2008.06.002

Tillier, A., Sirakov, N., Guadelli, A., Fernandez, P., Sirakova, S., Dimitrova, I., Ferrier, C., Guérin, G., Heidari, M., Krumov, I., Leblanc, J.-C., Miteva, V., Popov, V., Taneva, S., Guadelli, J.-L., 2017. Evidence of Neanderthals in the Balkans: The infant radius from Kozarnika Cave (Bulgaria). Journal of Human Evolution 111, 54–62. https://doi.org/10.1016/j.jhevol.2017.06.002

Trautmann, T., Dietrich, A., Stolz, W., Krbetschek, M.R., 1999a. Radioluminescence Dating: A New Tool for Quaternary Geology and Archaeology. Naturwissenschaften 86, 441–444. https://doi.org/10.1007/s001140050649

Trautmann, T., Krbetschek, M.R., Dietrich, A., Stolz, W., 1999b. Feldspar radioluminescence: a new dating method and its physical background. Journal of Luminescence 85, 45–58. https://doi.org/10.1016/S0022-2313(99)00152-0

Trautmann, T., Krbetschek, M.R., Dietrich, A., Stolz, W., 1998. Investigations of feldspar radioluminescence: potential for a new dating technique. Radiation Measurements 29, 421–425. https://doi.org/10.1016/S1350-4487(98)00012-2

Trinkaus, E., Moldovan, O., Milota, S., Bilgar, A., Sarcina, L., Athreya, S., Bailey, S.E., Rodrigo, R., Mircea, G., Higham, T., Ramsey, C.B., van der Plicht, J., 2003. An early modern human from the Pestera cu Oase, Romania. Proceedings of the National Academy of Sciences 100, 11231–11236. https://doi.org/10.1073/pnas.2035108100

Tsanova, T. 2006. Les débuts du Paléolithique supérieur dans l'Est des Balkans. Réflexion à partir de l'étude taphonomique et techno-économique des ensembles lithiques des sites de Bacho Kiro (couche 11), Temnata (couches VI et 4) et Kozarnika (niveau VII). Thèse de doctorat de l' Université Bordeaux 1, 543 pages.

Wintle, A.G., 1973. Anomalous fading of thermoluminescence in mineral samples. Nature 245, 143–144. https://doi.org/10.1038/245143a0

Wood, R., 2015. From revolution to convention: the past, present and future of radiocarbon dating. Journal of Archaeological Science 56, 61–72. https://doi.org/10.1016/j.jas.2015.02.019

Yi, S., Buylaert, J.-P., Murray, A.S., Thiel, C., Zeng, L., Lu, H., 2015. High resolution OSL and post-IR IRSL dating of the last interglacial–glacial cycle at the Sanbahuo loess site (northeastern China). Quaternary Geochronology 30, 200–206. https://doi.org/10.1016/j.quageo.2015.02.013

Figure

Click here to access/download;Figure;Figure1.png

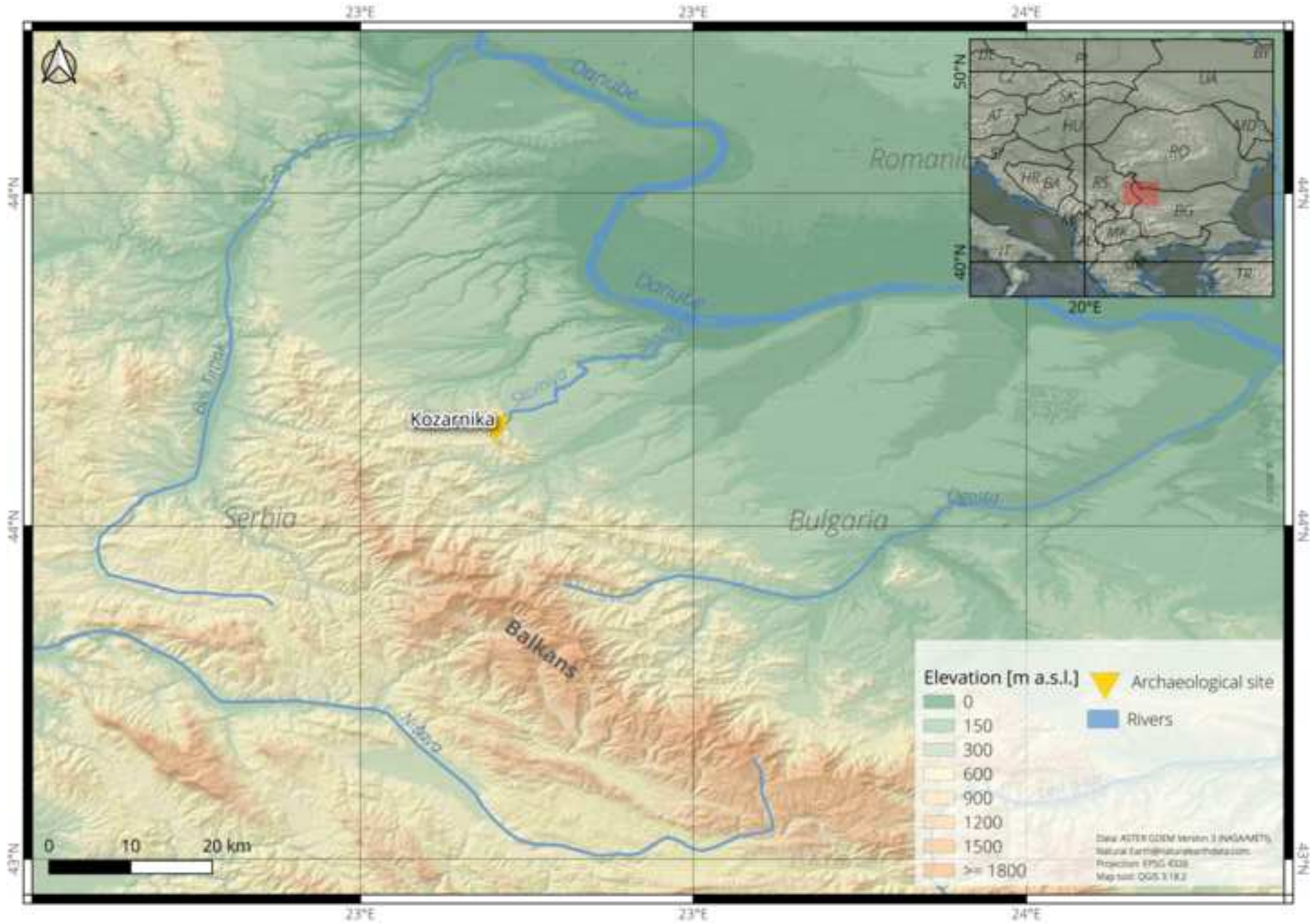

Figure

Click here to access/download;Figure;Figure2.pdf

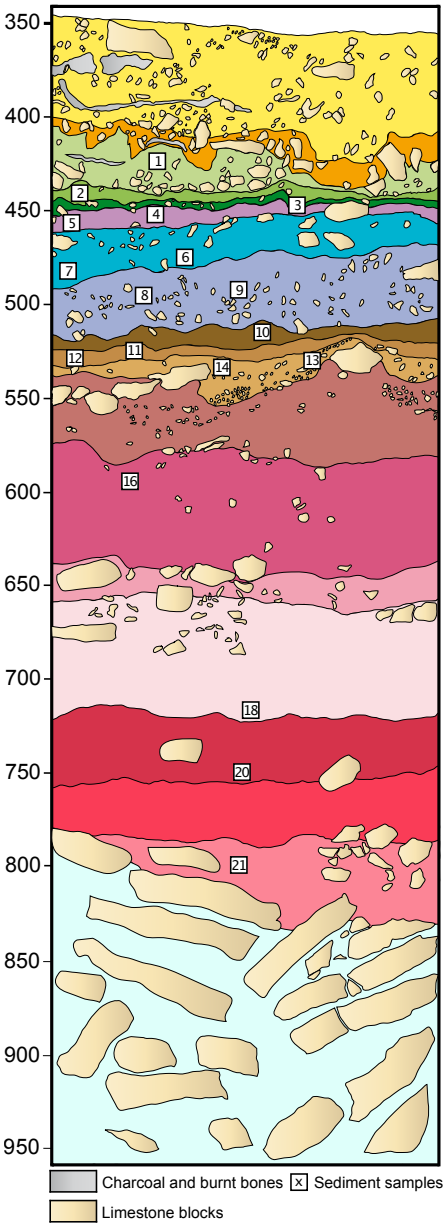


| | | OSL | IR-RF | VSL | pIRIR |
|---|---|---|---|---|---|
| | Koz 1 | 32±2 ka | | | |
| | Koz 2 | 30±2 ka | | | |
| 3a 3b | Koz 3 | 33±2 ka | | | |
| | Koz 4 | 33±2 ka | | | |
| 4 | Koz 5 | 35±2 ka | | | |
| 5a | Koz 6 | 49±4 ka | | | |
| 5b 5c 6/7 9ab | Koz 7 | 43±3 ka | | | |
| | Koz 8 | 53±3 ka | | | |
| 9c | Koz 9 | 51±3 ka | | | |
| 10a | Koz 10 | 59±4 ka | | | |
| 10b 10c | | | | | |
| | Koz 11 | | 201±17 ka | 321±77 ka | 161±13 ka |
| 11a | Koz 12 | | | | 199±12 ka |
| | Koz 13 | | | | 291±22 ka |
| | Koz 14 | | 279±29 ka | 324±94 ka | 281±19 ka |
| 11b | Koz 16 | | 337±23 ka | 419±137 ka | |
| 11c | | | | | |
| 12 | | | | | |
| | Koz 18 | | 290±18 ka | 377±113 ka | |
| 13a | | | | | |
| | Koz 20 | | 346±23 ka | | |
| 13b | | | | | |
| | Koz 21 | | 387±28 ka | 704±168 ka | |
| 13c | | | | | |
| 14, 15 & 16 | | | | | |

Figure

Click here to access/download;Figure;Figure3.

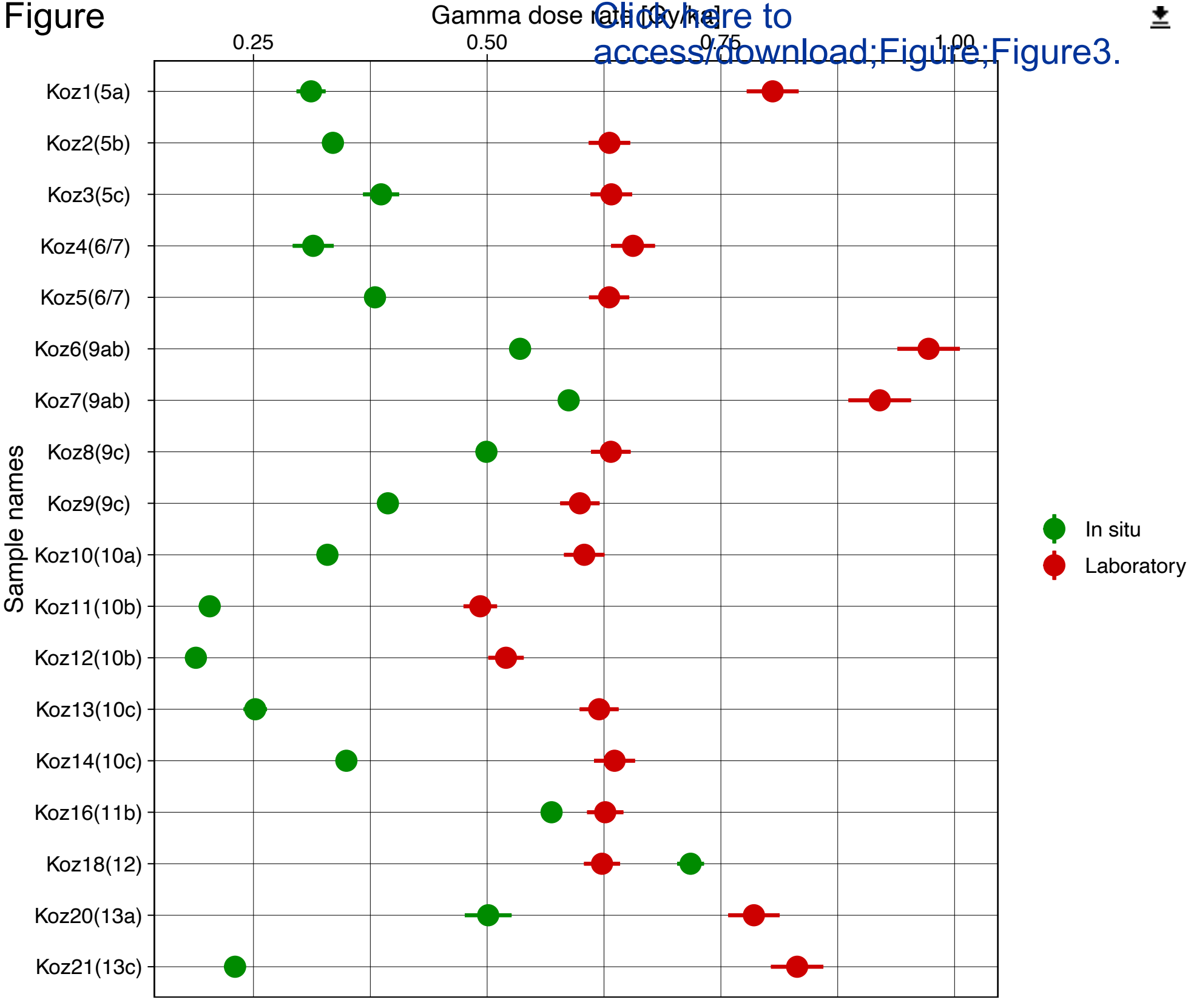

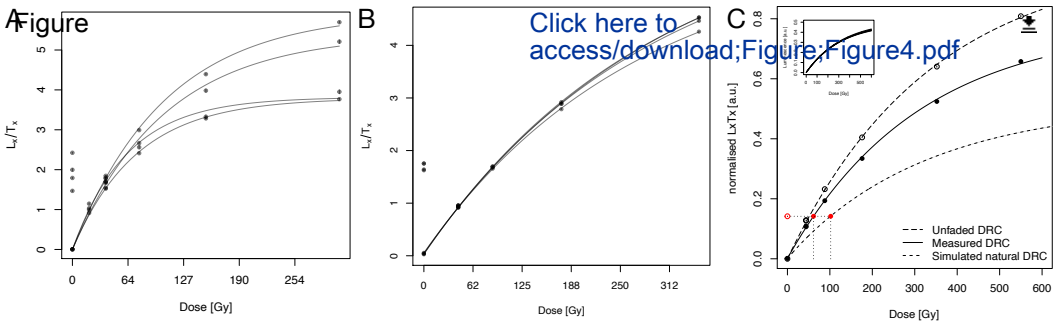
A
Figure
B
C
Click here to access/download;Figure;Figure4.pdf
$L_x/T_x$
Dose [Gy]
normalised $L_x/T_x$ [a.u.]
Unfaded DRC
Measured DRC
Simulated natural DRC

Figure

Figure



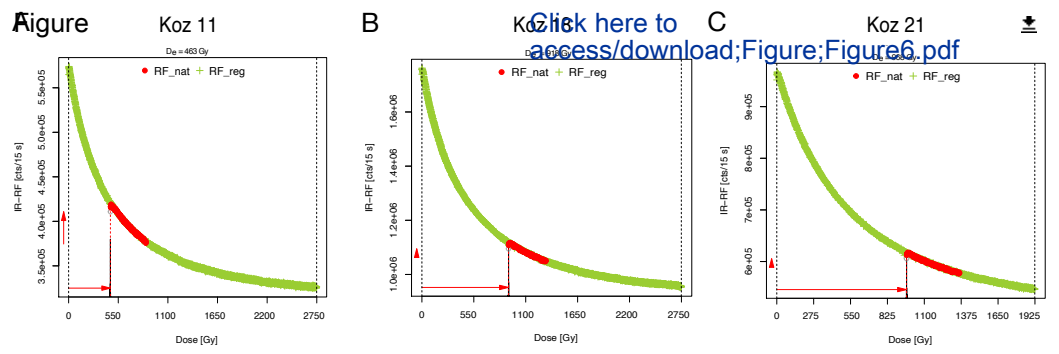

Figure

Click here to access/download;Figure;Figure8.pdf

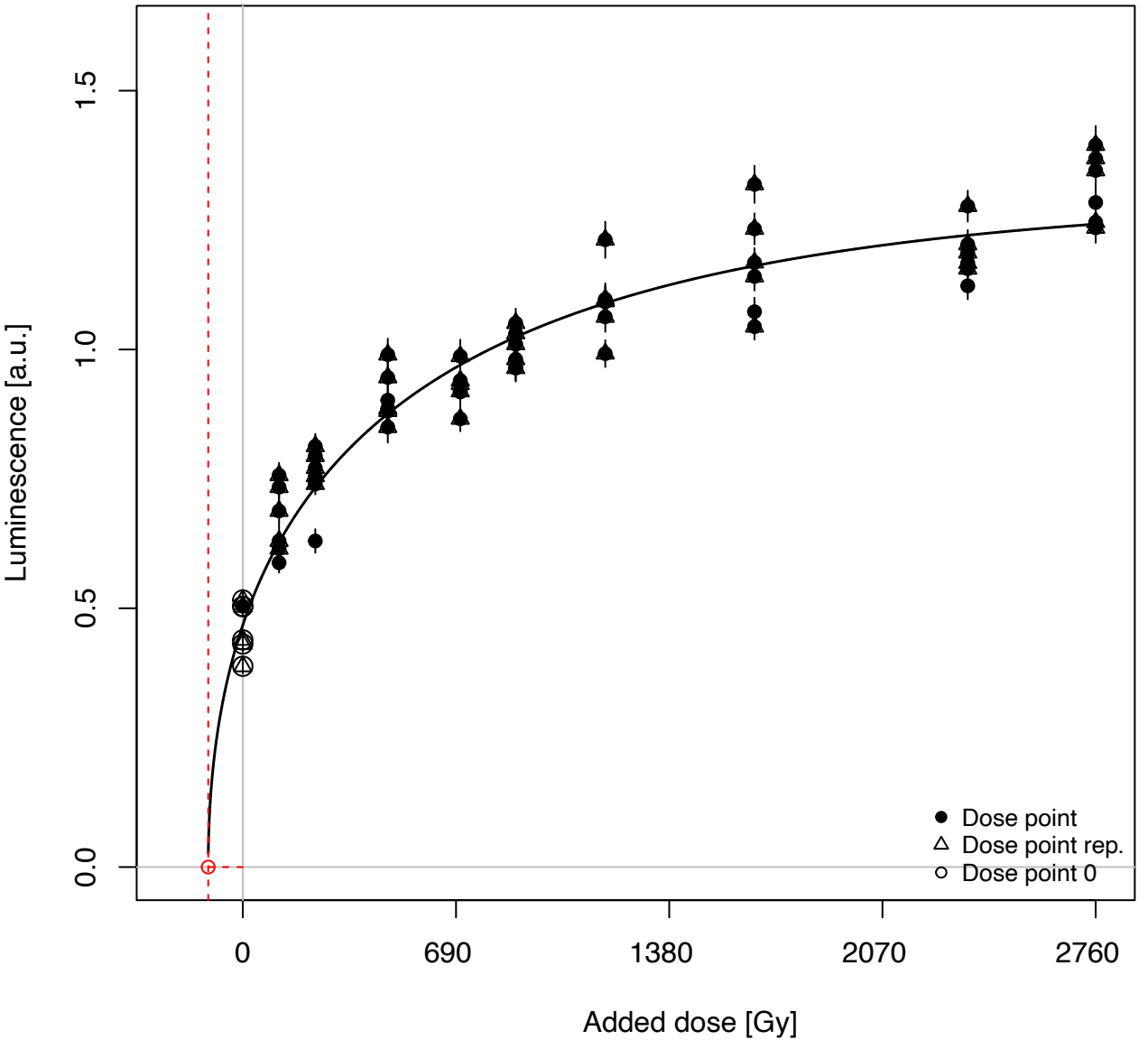

Figure